Efficient strength optimization of variable stiffness laminates using lamination parameters with global failure index

Hong, Zhi; Peeters, Daniël; Guo, Yujie

DOI
10.1016/j.compstruc.2022.106856

Publication date
2022

Document Version
Final published version

Published in
Computers and Structures

Computers and Structures 271 (2022) 106856

Contents lists available at ScienceDirect

Computers and Structures

journal homepage: www.elsevier.com/locate/compstruc

Efficient strength optimization of variable stiffness laminates using lamination parameters with global failure index

Zhi Hong [a,b,1,*], Daniël Peeters [b,2], Yujie Guo [c,3]

[a] School of Mechanical Engineering, Hangzhou Dianzi University, Hangzhou, PR China
[b] Aerospace Structures and Computational Mechanics, Faculty of Aerospace Engineering, Delft University of Technology, Delft, the Netherlands
[c] Key Laboratory of Fundamental Science for National Defense-Advanced Design Technology of Flight Vehicle, College of Aerospace Engineering, Nanjing University of Aeronautics and Astronautics, Nanjing, PR China

ARTICLE INFO

Article history:
Received 17 September 2021
Accepted 20 June 2022
Available online 30 July 2022

Keywords:
Novel composite laminates
Strength optimization
Global failure index
Variable fiber orientations
Lamination parameters

ABSTRACT

A computationally-efficient strength optimization method tailoring novel composite laminates using lamination parameters is developed. The method adopts a global *p*-norm approach to aggregate local failure indices into a global failure index, based on the Tsai-Wu failure criterion. For design purposes, the novel composite laminates are characterized via lamination parameters that can subsequently be transformed into locally variable fiber orientations in an existing three-step optimization method. An elliptical formulation of the conservative failure envelope is applied to represent the Tsai-Wu criterion in terms of lamination parameters. A lamination-parameter-based two-level approximation for the global failure index is derived, which guarantees the anticipated conservativeness and convexity in a gradient-based optimization framework. Numerical results show that the computational efficiency of the proposed strength optimization method improves remarkably with a proper value of *p*, compared to the existing local-based min-max method. The method is also shown to be robust and generate converged optimum designs even in the presence of stress concentrations and singularities.

1. Introduction

A basic requirement in structural design is to verify that the internal stresses and/or strains during operation do not exceed an allowable limit (i.e., the local failure strength) in order to guarantee the integrity of a structure. This process typically requires the computation of a stress or strain-based scalar quantity measured at every integration point in the structure under design loads and, subsequently, a verification that it does not exceed a critical value. This requirement can be incorporated in an optimal design problem as a local constraint or, in a strength-oriented formulation, as the design objective itself. A challenging issue with stress or strain-related optimization is that it often demands a significant computational effort, particularly as the number of degrees of freedom of the problem increases. The computational cost can be ascribed to the sensitivity analysis, which has to be executed for every local failure index to determine the change in failure index due to a variation of a design variable. An alternative approach, which has been implemented in order to reduce the computational cost, is to use a so-called *p*-norm formulation that aggregates the local values of the failure index into a single global failure measure for the whole structure. In contrast to minimizing the maximum failure index using the bound formulation [1], the use of a global (aggregate) *p*-norm failure index facilitates the implementation of the adjoint method for the design sensitivity analysis. Thus, the computational effort can be effectively reduced.

An early application of the *p*-norm approach was developed by Duysinx and Sigmund [2] in the context of topology optimization for isotropic materials. More recently, Holmberg et al. [3] proposed two different ways of clustering the stress constraints in the *p*-norm formulation, which effectively reduced the stress concentration in topology optimization. The *p*-norm aggregation has also been applied in a multi-constrained and multi-load topology optimization by Deng and Suresh [4]. In order to successfully constrain the maximum stress, Le et al. [5] proposed an adaptive normalization scheme as well as an interlacing regional stress measure for the *p*-norm stress constraint, which together provide direct control on the local stresses. A correction for the lower bound *p*-norm

* Corresponding author.
E-mail addresses: hongzhi6543@gmail.com (Z. Hong), D.M.J.Peeters@tudelft.nl (D. Peeters), yujieguo@nuaa.edu.cn (Y. Guo).
[1] Assistant professor in School of Mechanical Engineering, Hangzhou Dianzi University, PR China.
[2] Assistant professor, Faculty of Aerospace Engineering, Delft University of Technology, the Netherlands.
[3] Associate Professor in Key Laboratory of Fundamental Science for National Defense-Advanced Design Technology of Flight Vehicle, College of Aerospace Engineering, Nanjing University of Aeronautics and Astronautics, PR China.

https://doi.org/10.1016/j.compstruc.2022.106856
0045-7949/

Nomenclature

List of Acronyms

VSLs	variable stiffness laminates
CCSA	conservative convex separable approximation
LPs	lamination parameters
FEM	finite element method
KKT	Karush-Kuhn-Tucker
FI	failure index
MMA	method of moving asymptotes
SLSQP	sequential least square quadratic programming

stress constraint was proposed by Lee et al. [6] in topology optimization with the phase-field method. It was achieved by scaling the upper bound p-norm formulation with a scalar computed from the ratio between the lower bound p-norm formulation and its upper bound counter-part. Kiyono et al. [7] used a multi-p-norm to maximize the safety factor in topology optimization. Moreover, Verbart et al. [8] demonstrated that the lower bound p-norm function also has a relaxation effect on the stress constraint in topology optimization. Yang et al. [9] compared the stability transformation method-based stress correction scheme (using the p-norm function as one of the global stress measures) with the violated set enhanced stress measure in topology optimization. The results indicated that the former performs well in the volume minimization problem, whereas the latter behaves superior in the compliance minimization problem. Kambampati et al. [10] applied p-norm aggregation to constrain both stress and temperature fields in a multi-physics model in topology optimization.

The aforementioned research has focused mainly on isotropic materials. Notable applications of the p-norm approach to composite materials include a method based on the maximum strain or maximum stress criterion in combination with the discrete material optimization method [11]. In a follow-up research [12], the p-norm was used to separately take fiber failure and inter-fiber failure into account in the design of wind turbine blades made of composite material. More recently, Anderson et al. [13] applied a p-norm to aggregate the stress field of a composite wind turbine blade to improve the fatigue life via optimization. The aggregation is also utilized in an updated stress-based topology optimization of composite laminates using the layerwise theory, constrained by the Tsai-Hill criterion [14]. In the aforementioned works, the fiber angles are taken as the design variables in optimizing composite laminates. There is a recent publication by Montemurro and Catapano [15], where they introduce a framework to use polar parameters as design variables and B-spline to control the variable angle tows to optimize variable stiffness laminates. They also demonstrate an approach to optimize the strength of variable stiffness composites using polar parameters in the framework of the first-order shear deformation theory [16]. A high value of p is shown to be adopted in their framework utilizing the Sequential Least Square Quadratic Programming [17]. Many details on the relevant implementation can be found in [18].

For optimal design of variable stiffness laminates, one commonly-used framework is the three-step optimization method [1,19–25]. In the first step of the method, the optimal lamination parameters are identified. Subsequently, in the second step, the fiber angles in each ply of a composite laminate are retrieved from the optimal lamination parameters. Finally, in the third step, the fiber paths of the variable stiffness laminates (VSLs) are constructed based on the fiber angles obtained.

Although the three-step optimization framework has proven to be an efficient and versatile approach for designing advanced composite materials, we want to explore an effective numerical approach to overcome the bottleneck of the strength optimization on its expensive computational cost. The p-norm aggregation has hitherto not been investigated within this framework, where the lamination parameters are the design variables. In view of this, we want to introduce an approach with details on how to carry out strength optimization of variable stiffness laminates using the p-norm formulation to speed up the calculation of [1] in our three-step optimization framework. The aim of this work is two-fold: (i) to develop and implement a p-norm approach for efficient strength optimization of VSLs composites using the lamination parameters as design variables, and (ii) to compare the performance of the p-norm approach with an existing min-max formulation [1] within the same three-step optimization framework.

For the accuracy and ease of implementation, the Tsai-Wu failure criterion is used in the present work. In order to fit and simplify the fiber angle-based Tsai-Wu failure criterion with respect to the lamination parameters, an elliptical formulation of the conservative failure envelope [1] is employed. According to our previous study on strength-related optimization [26], we found the stress field and its sensitivity field are not continuous in the space. This causes the optimal design mesh-dependent in strength optimization. Therefore, we deal with this problem by proposing a hybrid interpolation scheme in terms of the analysis and optimization. In addition, we want to come up with a convex approximation for the p-norm failure index with respect to the lamination parameters, which is essential in our framework. The p-norm failure index is obtained by aggregating the nodal indices with a critical failure surface that accounts for all possible angle orientations. This approach can be applied to other failure criteria. In the first step of the three-step optimization method, the original optimization problem is replaced by an approximate sub-problem, which requires the derivation of a convex, two-level approximation for the p-norm failure index. Finally, the strength optimization is resolved with a predictor-corrector interior point method [27] within the framework of the conservative convex separable approximation (CCSA) [28].

The structure of this work is as follows: Section 2 describes the lamination parameters and the structural analysis of the VSLs using the finite element method. The proposed p-norm failure index and its convex two-level approximation are also derived in this section. The formulation of the strength optimization and the corresponding methods to solve the problem are discussed in Section 3. In Section 4, numerical results on the effect of p and the mesh convergence of the optimal solutions, and the comparison with the local min-max bound formulation are demonstrated for a square plate with a cut-out. Another numerical case of an L-shaped plate is tested in Section 5 to examine the performance of the proposed strength optimization in the presence of stress singularity in detail. Finally, concluding remarks are provided in Section 6.

2. Strength analysis for variable stiffness laminates and the global failure index

The structural analysis of the VSLs is undertaken using the finite element method, which provides the local state of stress in a structure or structural component under design loads. The relative

strength of the VSLs, which compares a given state of stress with a maximum allowable value, is represented locally by a failure index based on the Tsai-Wu failure criterion. A global failure index, formulated using the *p*-norm formulation, is introduced here, and is henceforth referred to as the "*p-norm failure index*". Subsequently, a convex two-level approximation is derived for this *p*-norm failure index to ensure both the convexity and conservativeness of the sub-problem associated with the strength optimization, required by the convex optimization framework. Details about the structural analysis and *p*-norm failure index are described in this section.

2.1. Lamination parameters

The lamination parameters (LPs), which are the design variables in the first-step optimization, are particularly suited for identifying the effective properties of layer-wised composite laminate without the need to specify the ply angles [29,30]. The effective stiffness of the VSLs can be directly calculated through the LPs. In particular, the in-plane stiffness matrix $\mathbf{A}$ can be calculated by four in-plane LPs (V_1, V_2, V_3, V_4), the thickness of the laminate h and five matrix constants $(\mathbf{\Gamma}_0, \mathbf{\Gamma}_1, \mathbf{\Gamma}_2, \mathbf{\Gamma}_3, \mathbf{\Gamma}_4)$ using

$$\mathbf{A} = h(\mathbf{\Gamma}_0 + V_1\mathbf{\Gamma}_1 + V_2\mathbf{\Gamma}_2 + V_3\mathbf{\Gamma}_3 + V_4\mathbf{\Gamma}_4). \tag{1}$$

The parameters (V_1, V_2, V_3, V_4) are defined based on the classical lamination theory as

$$(V_1, V_2, V_3, V_4) = \int_{-\frac{1}{2}}^{\frac{1}{2}} (\cos 2\theta(\bar{z}), \sin 2\theta(\bar{z}), \cos 4\theta(\bar{z}), \sin 4\theta(\bar{z}))d\bar{z}, \tag{2}$$

where $\bar{z}$ is the normalized position in the thickness direction with the center defined at the mid-plane and $\theta(\bar{z})$ is the fiber angle at $\bar{z}$.

Similarly, the out-of-plane stiffness matrix $\mathbf{D}$ can be calculated by four out-of-plane LPs. More information about the LPs and the corresponding matrix constants can be found in [31].

Since the LPs are calculated from the trigonometric functions in Eq. (2), each pair of the LPs is confined within a feasible region. For the in-plane LPs, the feasible domain is given by

$$2V_1^2(1 - V_3) + 2V_2^2(1 + V_3) + V_3^2 + V_4^2 - 4V_1V_2V_4 \leqslant 1, \tag{3a}$$
$$V_1^2 + V_2^2 \leqslant 1, \tag{3b}$$
$$-1 \leqslant V_3 \leqslant 1. \tag{3c}$$

The current work aims to design symmetric and balanced laminates. This aligns with the design principle in the aerospace industry. Two lamination parameters become zero ($V_2, V_4 = 0$) due to the stacking sequence. The feasible domain simplifies to

$$2V_1^2 - V_3 - 1 \leqslant 0, \tag{4a}$$
$$V_3 - 1 \leqslant 0. \tag{4b}$$

This would be the feasible domain for zero membrane/bending coupling and membrane orthotropic laminates, which is a sufficient condition to generate symmetric and balanced laminates. By using this, we exclude the potential designs which do not correlate with symmetric and balanced stacks in the first-step optimization. In the angle retrieval step, we can develop symmetric and balanced layups based on the optimal design in the first-step to guarantee the specific stacking sequence. (method can be found in [25]). We would like to note here that the feasible domain of the lamination parameters is an approximated convex-hull [32], where the values in a small fraction of the domain can not be mapped into physical carbon fiber lay-ups [33]. Since this drawback alleviates effectively when the number of design layers is high, we regard such constraints as valid in formulating the optimization problem.

As the in-plane stiffness matrix $\mathbf{A}$ is linear with respect to the LPs (see Eq. (1)), the convexity of a functional with respect to $\mathbf{A}$ is preserved in the LP space. This convexity is a significant advantage of taking the LPs as design variables instead of the fiber angles in all layers. Furthermore, the number of design variables can be reduced to a maximum of 4 at each design point for in-plane cases, regardless of the number of design layers for balanced laminates. A similar rule applies to the out-of-plane cases.

2.2. Structural analysis of variable stiffness laminates

As described in our research [26], the strength related optimization behaves mesh-dependent in structural design. The reason is that the sensitivity of the strength obtained from the FEM model is not continuous [26,8]. Hence, we propose a well-behaved hybrid interpolation scheme in the finite element method (FEM) model after numerous trial and error in order to depress such an effect. Specifically, we utilize a higher order element to smoothen the strength field in the FEM model compared to the constant-strain triangle element in [1]. An 8-noded serendipity element [34] is applied, which aims to enhance the continuity of the stress field. This continuity is desirable when calculating the sensitivity of the stress-based objectives or constraints. For the design purpose, both the material stiffness and the local strength constraint are defined on the vertices of the serendipity element, which are also named as the design nodes (see Fig. 1). The interpolation of the failure indices between the Gauss points and the design nodes is achieved using a linear quadrilateral element, referred to as "*design and interpolation element*". By using different elements for analysis and interpolation respectively, not only the local strength can be well-defined, the number of strength constraints and design variables can also be reduced.

To evaluate the stiffness matrix in one element, the material stiffness $\mathbf{A}_g$ at a Gauss point g is obtained using a reciprocal interpolation,

$$\mathbf{A}_g^{-1} = \sum_{i=1}^{n} R_{i,g}\mathbf{A}_i^{-1}, \tag{5}$$

where $\mathbf{A}_i$ is the stiffness matrix at the i^{th} design node in the element, $R_{i,g}$ is the linear shape function of the i^{th} design node in the interpolation element evaluated at the g^{th} Gauss point, and n is the total number of design nodes. In the remainder of the text, the subscript g refers to the value at the g^{th} Gauss point, and the subscript i indicates the value at the i^{th} design node.

Once the stiffness matrix is computed for each element, the global stiffness matrix $\mathbf{K}$ can be obtained following a standard assembly procedure. The displacement $\vec{u}$ for each degree of freedom can be obtained through

$$\mathbf{K}\vec{u} = \vec{f}, \tag{6}$$

where $\vec{f}$ is the external load vector. Thereafter, the strain or stress of the VSLs at the Gauss points can be obtained for the calculation of the relative strength.

2.3. p-norm failure index

The elliptical formulation of the conservative failure envelope [1] is applied in this study to achieve a conservative approximation of the safe region given by the Tsai-Wu failure criterion. The rationale is to approximate the safety region in the strain space using a quadratic function for the most critical fiber angles. This is necessary for use in conjunction with lamination parameters, since the fiber angles, required by the Tsai-Wu failure criterion, are not available during the first step of the optimization process (they

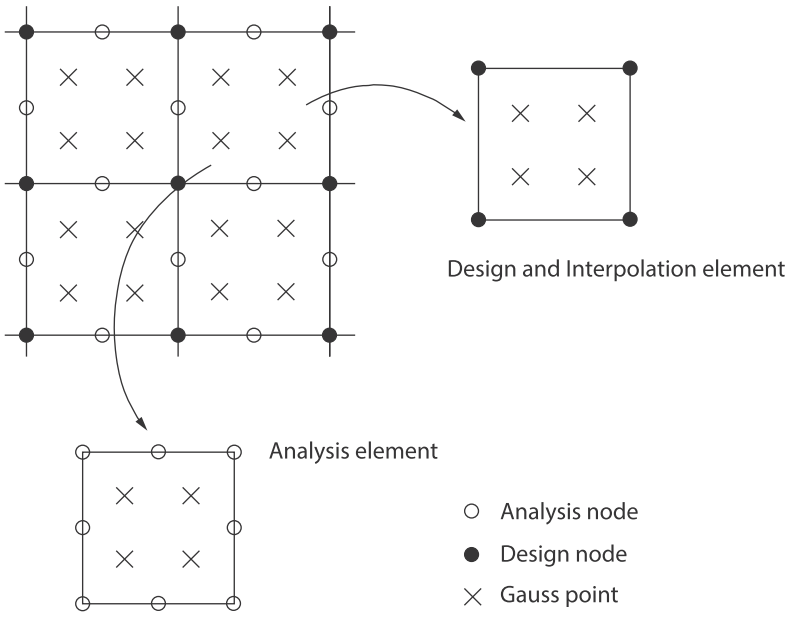

Fig. 1. Analysis, and design and interpolation element in the finite element model.

are obtained during a subsequent step after the optimal lamination parameters have been identified). Another type of failure index in the framework of first-order shear deformation theory is introduced by Izzi et al. [17]. In this approach, the failure index is obtained by integrating layerwise carbon fiber failure indices through the thickness. The advantage of this approach is that it simplifies a complex physical mechanism, and is precise for the composite fiber layers. We recommend this approach as long as the inter-laminate matrix is robust enough. In our work, the local failure index r is calculated as the largest root of the Tsai-Wu failure envelope at each Gauss point as

$$a_0 r^2 + a_1 r + a_2 = 0, \tag{7}$$

where the coefficients a_0, a_1 and a_2 are given as follows:

$$a_0 = C_0, \tag{8a}$$
$$a_1 = C_I e_I + C_{II} e_{II}, \tag{8b}$$
$$a_2 = C_{I,I} e_I^2 + C_{II,II} e_{II}^2 + 2C_{I,II} e_I e_{II}. \tag{8c}$$

In the previous expression, e_I and e_{II} are the principal strains, where the subscripts I and II refer to the maximum and minimum strain directions, respectively. The coefficients $C_0, C_I, C_{II}, C_{I,I}, C_{II,II}$ and $C_{I,II}$ are obtained from the material properties (strength and stiffness). Details associated with the calculation are discussed in Khani [35]. The critical envelope (occurence of failure) is defined by $r = 1$ and the safe region, where no failure occurs, is given by $r \leqslant 1$.

Next, the nodal failure indices are determined by interpolation from the values at the Gauss points. With this interpolation, both the local failure indices and the design variables are defined at the design nodes. The failure index at the i^{th} design node is recovered using an equivalent formulation as the one described in Nagy et al. [36], which results in

$$r_i = \frac{\int r R_i d\Omega}{\int R_i d\Omega}, \tag{9}$$

where R_i is the shape function of an interpolation element associated with the design nodes and Ω denotes the domain occupied by the structure.

Once the nodal failure index is obtained, the p-norm failure index r^{PN} can be estimated by

$$r^{PN} = \left(\frac{1}{|\Omega|}\int_\Omega r^p d\Omega\right)^{\frac{1}{p}} \approx \left(\frac{1}{|\Omega|}\sum_{i=1}^{n} |\Omega_i| r_i^p\right)^{\frac{1}{p}}, \tag{10}$$

where $|\Omega| = \int_\Omega d\Omega$is the area of the entire design domain, p is the coefficient of the p-norm, Ω_i is a domain associated with the i^{th} design node. It is obtained through $\Omega_i = \sum_{g=1}^{n_i} w_{i,g} \|\mathbf{J}_{i,g}\|$, where $w_{i,g}, \|\mathbf{J}_{i,g}\|$ are the weight and the determinant of Jacobian matrix respectively of the g^{th} Gauss point connected with the i^{th} design node in the Gaussian quadrature, n_i is the number of Gauss points connected with the i^{th} design node.

2.4. Convex two-level approximation for the p-norm failure index

In order to implement the optimization algorithm, it is convenient to develop a two-level approximation, which reduces redundant computational work of the sensitivity analysis by updating hierarchically only if improvement is achieved in one level [20,37–39]. In this section, a convex two-level approximation is derived for the p-norm failure index.

In the first level approximation, the p-norm failure index is expanded with respect to the in-plane stiffness, which is to be optimized for maximum strength. According to Eq. (7), the local failure index r is a function of local strain $\vec{e}_g$, thus a function of $\mathbf{A}_g$ as well. Therefore, r_g can be locally approximated at a Gauss point g by

$$r_g \approx \mathbf{\Phi}_g : \mathbf{A}_g^{-1}. \tag{11}$$

The coefficient matrix $\mathbf{\Phi}_g$ is a symmetric matrix calculated by

$$\mathbf{\Phi}_g = \frac{1}{2}\left(\vec{N}_g \vec{q}_g^T + \vec{q}_g \vec{N}_g^T\right), \tag{12}$$

with $\vec{q}_g = \frac{\partial r_g}{\partial \vec{e}_g}$ being the sensitivity of r_g with respect to $\vec{e}_g$, and $\vec{N}_g$ is the resultant internal force. Note that Eq. (11) is called "*locally approximated*" as it only considers the variation of the stiffness matrix $\mathbf{A}_g^{-1}$. The change of the internal force $\vec{N}_g$ and the global effect of load redistribution associated with $\vec{N}_g$ in $\mathbf{\Phi}_g$ (Eq. (12))) due to the variation of $\mathbf{A}_g$ still needs to be calculated through the adjoint method. Details about the derivation of Eq. (11) are omitted here for the sake of brevity (see Khani et al. [1]).

The nodal failure index can be obtained by substituting Eq. (11) into Eq. (9) and using Gaussian quadrature, resulting in

$$r_i = \frac{\sum_{g=1}^{n_g}\left(\mathbf{\Phi}_g : \mathbf{A}_g^{-1}\right) R_{i,g} w_g \|\mathbf{J}_g\|}{\sum_{g=1}^{n_g} R_{i,g} w_g \|\mathbf{J}_g\|}, \tag{13}$$

where n_g is the total number of Gauss points in the model, $\|\mathbf{J}_g\|$ is the determinant of the Jacobian matrix in the element, $R_{i,g}$ is the shape function evaluated at the Gauss point and w_g is the weight factor for the Gaussian quadrature.

After substituting Eq. (5) into Eq. (13), the following expression is obtained:

$$r_i = \frac{\sum_{g=1}^{n_g}\left(R_{i,g} w_g \|\mathbf{J}_g\| \mathbf{\Phi}_g : \left(\sum_{j=1}^{n} R_{j,g} \mathbf{A}_j^{-1}\right)\right)}{\sum_{g=1}^{n_g} R_{i,g} w_g \|\mathbf{J}_g\|}. \tag{14}$$

By rearranging the terms, the formulation for the nodal failure index is expressed in terms of the nodal in-plane stiffness $\mathbf{A}_j$ as

$$r_i = \sum_{j=1}^{n} \mathbf{\Phi}_{i,j} : \mathbf{A}_j^{-1}, \tag{15}$$

where the coefficient matrix $\mathbf{\Phi}_{i,j}$ is given as

$$\mathbf{\Phi}_{i,j} = \frac{\sum_{g=1}^{n_g} R_{i,g} w_g \|\mathbf{J}_g\| R_{j,g} \mathbf{\Phi}_g}{\sum_{g=1}^{n_g} R_{i,g} w_g \|\mathbf{J}_g\|}. \tag{16}$$

The local approximation for r^{PN} can be subsequently obtained by substituting Eq. (15) into Eq. (10), which leads to

$$r^{PN}\left(\mathbf{A}^{-1}\right) = \sum_{j=1}^{n} \mathbf{\Phi}_j^{PN} : \mathbf{A}_j^{-1}, \tag{17}$$

where $\mathbf{\Phi}_j^{PN}$ is obtained through the chain rule as follows:

$$\mathbf{\Phi}_j^{PN} = \frac{\partial r^{PN}}{\partial \mathbf{A}_j^{-1}} = \sum_{i=1}^{n} \frac{\partial r^{PN}}{\partial r_i} \frac{\partial r_i}{\partial \mathbf{A}_j^{-1}}. \tag{18}$$

Hence, combining Eq. (10) and Eq. (15), the complete formulation of $\mathbf{\Phi}_j^{PN}$ is given by

$$\mathbf{\Phi}_j^{PN} = \sum_{i=1}^{n}\left(\frac{1}{|\Omega|}\sum_{i=1}^{n}|\Omega_i| r_i^p\right)^{\left(\frac{1}{p}-1\right)}\left(\frac{|\Omega_i|}{|\Omega|} r_i^{(p-1)}\right)\mathbf{\Phi}_{i,j}. \tag{19}$$

The coefficient matrix $\mathbf{\Phi}_j^{PN}$ is not guaranteed to be a positive semi-definite matrix. In order to guarantee the convexity of the first level approximation, spectral decomposition is applied to convexify Eq. (17), which leads to

$$r^{PN}\left(\mathbf{A}, \mathbf{A}^{-1}\right) \approx \sum_{j=1}^{n}\left(\Psi_j^{PN}\right)^{-} : \mathbf{A}_j + \sum_{j=1}^{n}\left(\mathbf{\Phi}_j^{PN}\right)^{+} : \mathbf{A}_j^{-1}, \tag{20}$$

where $\left(\mathbf{\Phi}_j^{PN}\right)^{+}$ is the positive definite part of $\mathbf{\Phi}_j^{PN}$ obtained from the spectral decomposition, and $\sum_{j=1}^{n}\left(\Psi_j^{PN}\right)^{-} : \mathbf{A}_j$ is the linear expansion of the corresponding non-definite part. Details on the implementation of this spectral decomposition are described by Khani et al. [1].

Finally, the complete convex first level approximation of the p-norm failure index, accounting for the linear expansion and load redistribution part obtained through the adjoint method, is

$$r^{PN(I)}\left(\mathbf{A}, \mathbf{A}^{-1}\right) = \sum_{j=1}^{n} \Psi_j^{PN} : \mathbf{A}_j + \sum_{j=1}^{n}\left(\mathbf{\Phi}_j^{PN}\right)^{+} : \mathbf{A}_j^{-1}, \tag{21}$$

where Ψ_j^{PN} includes $\left(\Psi_j^{PN}\right)^{-}$, the linear expansion of $\mathbf{\Phi}_j^{PN}$ in $r^{PN}\left(\mathbf{A}^{-1}\right)$ (Eq. (17)) with respect to $\mathbf{A}_j$, and the load redistribution part in $\mathbf{\Phi}_j^{PN}$ calculated by solving the adjoint problem. More details are discussed in Appendix A.

The second level approximation for the p-norm failure index $r^{PN(II)}\left(\vec{V}\right)$ is formulated in terms of the lamination parameters $\vec{V}$ as

$$r^{PN(II)}\left(\vec{V}\right) \approx r_0^{PN(I)}\left(\vec{V}^0\right) + \left(\vec{g}^{PN}\right)^T \Delta\vec{V} + \frac{1}{2}\Delta\vec{V}^T \mathbf{H}^{PN} \Delta\vec{V}, \tag{22}$$

where $\vec{V}$ is a vector that collects all lamination parameters at all design nodes (i.e., $\vec{V} = [V_{\beta,i}]$, with $\beta = 1, 3$ and $i = 1, \ldots, n$), $\vec{V}^0$ is a design point about which the approximation is being made, $\Delta\vec{V} = \vec{V} - \vec{V}^0, r_0^{PN(I)}\left(\vec{V}^0\right)$ is the value of $r^{PN(I)}$ at the approximation point $\vec{V}^0, \vec{g}^{PN}$ is the gradient of $r^{PN(I)}$ with respect to the lamination parameters at $\vec{V}^0$, and $\mathbf{H}^{PN}$ is the Gauss-Newton part of the Hessian matrix [37].

Denote as $k = 1, \ldots, 2n$ an index that corresponds to a unique combination of a pair of indices $\beta = 1, 3$ and $i = 1, \ldots, n$ such that $V_k = V_{\beta,i}$. The calculation of the k^{th} component of $\vec{g}^{PN}$ and the corresponding diagonal component of $\mathbf{H}^{PN}$ is as follows:

$$g_k^{PN} = \Psi_i^{PN} : \frac{\partial \mathbf{A}_i}{\partial V_k} + \left(\mathbf{\Phi}_i^{PN}\right)^{+} : \frac{\partial \mathbf{A}_i^{-1}}{\partial V_k}, \tag{23}$$

and

$$H_{k,k}^{PN} = \left(\mathbf{\Phi}_i^{PN}\right)^{+} : \frac{\partial^2 \mathbf{A}_i^{-1}}{\partial V_k^2}. \tag{24}$$

3. Strength optimization with p-norm failure index

The formulation and the algorithm to resolve the strength optimization problem with a p-norm failure index are described in this section. The p-norm failure index is the objective and the feasible domain of the lamination parameters at each design node are taken as constraints. Consequently, the formulation of the optimization takes the following form:

$$\min_{\vec{V}_1, \vec{V}_3} \quad r^{PN} \tag{25a}$$

$$\text{subject to} \quad 2V_{1,i}^2 - V_{3,i} - 1 \leqslant 0, \tag{25b}$$

$$V_{3,i} - 1 \leqslant 0 \qquad i = 1 \ldots n. \tag{25c}$$

The aforementioned second level approximation $r^{PN(II)}$ is employed to set up the sub-problem that replaces the original optimization problem. The Karush-Kuhn-Tucker (KKT) condition of the sub-problem is addressed using Mehrotra's predictor-corrector interior point method [27] due to its fast convergence rate. The detailed process to formulate the Schur complement follows the procedure in Hong and Abdalla [40], which is omitted here for conciseness. The conservative convex separable approximation (CCSA) [28] is chosen as the optimization framework to control the convergence in each level.

The conservativeness of the approximation required in the CCSA aims to ensure the value at the new optimum obtained from the approximation is higher than that from the finite element model. Under this condition, the optimal solution obtained from the

subproblem improves the design on the feasible side, which finally leads to a converged solution. To guarantee this characteristic in the two-level approximation for r^{PN}, extra damping functions, selected to be convex and separable, are supplemented to each level. To this end, the first level approximation together with damping is denoted as

$$\check{r}^{PN(I)}\left(\mathbf{A},\mathbf{A}^{-1}\right)=r^{PN(I)}\left(\mathbf{A},\mathbf{A}^{-1}\right)+\rho^{(I)}d^{(I)}\left(\mathbf{A},\mathbf{A}^{-1}\right), \tag{26}$$

where $\rho^{(I)}\in\mathbb{R}^{+}$ is the damping factor in the first level to scale the effect of the damping function $d^{(I)}$. The function $d^{(I)}\left(\mathbf{A},\mathbf{A}^{-1}\right)$ is given by

$$d^{(I)}\left(\mathbf{A},\mathbf{A}^{-1}\right)=\sum_{i=1}^{n}o_i\left(\mathbf{A}_i:\mathbf{A}_{0,i}^{-1}+\mathbf{A}_{0,i}:\mathbf{A}_i^{-1}-2\mathbf{I}:\mathbf{I}\right), \tag{27}$$

where $\mathbf{I}$ is the identity matrix, $\mathbf{A}_{0,i}$ is the in-plane stiffness at the approximation point $\vec{V}^0$ and at the design node i, o_i is the weight factor for the terms at each design node with $o_i=\frac{|\Omega_i|}{|\Omega|}$. The value of $d^{(I)}\left(\mathbf{A},\mathbf{A}^{-1}\right)$ and its first derivative at the approximation point are zero, which ensures Eq. (26) is still a valid approximation.

The corresponding second level approximation with damping added is expressed as

$$\check{r}^{PN(II)}\left(\vec{V}_1,\vec{V}_3\right)=r^{PN(II)}\left(\vec{V}_1,\vec{V}_3\right)+\rho^{(II)}d^{(II)}\left(\vec{V}_1,\vec{V}_3\right), \tag{28}$$

where $\rho^{(II)}\in\mathbb{R}^{+}$ is the damping factor in the second level to scale the effect of the damping function $d^{(II)}$. The function $d^{(II)}\left(\vec{V}_1,\vec{V}_3\right)$ in this level is formulated as follows:

$$d^{(II)}\left(\vec{V}_1,\vec{V}_3\right)=\sum_{i=1}^{n}o_i\left(V_{1,i}-V_{1,i}^0\right)^2+\sum_{i=1}^{n}o_i\left(V_{3,i}-V_{3,i}^0\right)^2, \tag{29}$$

where $V_{1,i}^0$ and $V_{3,i}^0$ are the lamination parameters at the approximation point $\vec{V}^0$ at the design node i.

The flowchart of the optimization in the CCSA is illustrated in Fig. 2. The associated procedure is summarized in Algorithm 1. The optimization loop connected to the first level approximation is named as the "Level 1 optimization", which is in essence the outer loop of the CCSA. Similar rule applies to the "Level 2 optimization", which correlates with the inner loop of the CCSA. The sensitivity analysis and the convergence check using FEM analysis is called "Level FEM".

Algorithm 1. Strength optimization with p-norm failure index

1 Initialize $\vec{V}^0,\rho^{(I)},\rho^{(II)}$ and set the tolerance of stopping criterion in Level 1, Level 2 and Level FEM optimization $\eta^{(I)},\eta^{(II)},\eta^{(0)}$, respectively;
2 Start FE analysis to calculate r^{PN} and its sensitivity $\left(\mathbf{\Phi}_j^{PN}\right)^{+},\Psi_j^{PN}$;
3 Set up Level 1 approximation $\check{r}^{PN(I)}$;
4 Set up Level 2 approximation $\check{r}^{PN(II)}$. Build up the subproblem with $\check{r}^{PN(II)}$ and solve it with the predictor-corrector interior point method;
5 Update damping factor $\rho^{(II)}$;
6 Check if $\check{r}^{PN(I)}$ improves. If $\Delta\check{r}^{PN(I)}\leqslant\eta^{(I)}$, solution accepted and update $\check{r}^{PN(I)}$. Otherwise go back to step 4;
7 Check the convergence of $\check{r}^{PN(I)}$. If $|\Delta\check{r}^{PN(I)}|\leqslant\eta^{(I)}$, update $\rho^{(I)}$. Otherwise, go back to step 4;
8 Check if r^{PN} from the Level FEM is reduced. If $\Delta r^{PN}\leqslant\eta^{(0)}$, solution accepted. Otherwise, go back to step 3;
9 Check the convergence of r^{PN} from the Level FEM. If $|\Delta r^{PN}|\leqslant\eta^{(0)}$, optimal result $\vec{V}^*$ is obtained. Otherwise, go back to step 2.

In this work, the tolerance for the Level 2 optimization is $\eta^{(II)}=10^{-10}$. The tolerance for the Level 1 optimization is $\eta^{(I)}=10^{-3}$ and the variation in the Level 1 approximation $\Delta\check{r}^{PN(I)}$ is given by

$$\Delta\check{r}^{PN(I)}=r^{PN(I)}\left(\left(\vec{V}^{k+1}\right)^{*}\right)-r^{PN(I)}\left(\left(\vec{V}^{k}\right)^{*}\right), \tag{30}$$

where $\left(\vec{V}^{k}\right)^{*}$ is the optimal solution obtained in the k^{th} Level 1 iteration. Once the $(k+1)^{\text{th}}$ Level 1 optimization converges, the in-plane stiffness $\mathbf{A}$ and its inverse $\mathbf{A}^{-1}$ in $r^{PN(I)}$ (Eq. (21)) are updated.

The tolerance for the convergence of the Level FEM optimization is $\eta^{0}=10^{-3}$ and the variation in this level $\Delta\check{r}^{PN}$ is

$$\Delta\check{r}^{PN}=r^{PN}\left(\left(\vec{V}^{l+1}\right)^{*}\right)-r^{PN}\left(\left(\vec{V}^{l}\right)^{*}\right), \tag{31}$$

where $\left(\vec{V}^{l}\right)^{*}$ is the optimal solution obtained at the l^{th} Level FEM iteration.

The damping factors $\rho^{(I)}$ and $\rho^{(II)}$ are updated as follows:

$$\rho^{(\alpha),t+1}=\delta\rho^{(\alpha),t}, \tag{32}$$

where the superscript $\alpha=I,II$ and t is the iteration number in the α^{th} level optimization. To calculate δ, a parameter $\underline{\delta}$ is computed first at the optimal solution $\vec{V}^*$ in the α^{th} level

$$\underline{\delta}=\frac{r^{PN(\alpha-1)}\left(\vec{V}^*\right)-\check{r}^{PN(\alpha)}\left(\vec{V}^*\right)}{\rho^{(\alpha),t}d^{(\alpha)}\left(\vec{V}^*\right)}+1. \tag{33}$$

Then δ in the α^{th} level is obtained using:

$$\delta=\begin{cases}\check{\delta} & \underline{\delta}>\check{\delta}\\ \underline{\delta} & \hat{\delta}<\underline{\delta}\leqslant\check{\delta}\\ \hat{\delta} & 1<\underline{\delta}\leqslant\hat{\delta}\\ 1+0.5\tanh(2\underline{\delta}-2) & \underline{\delta}\leqslant 1,\end{cases} \tag{34}$$

where $\check{\delta}$ and $\hat{\delta}$ are two adjustable parameters. These two parameters intend to make the damping factor increase by a reasonable ratio in each iteration, neither dramatically large nor small. The function for the $\underline{\delta}\leqslant 1$ case constrains the damping factor $\rho^{(\alpha)}$ to decrease no further than to half of the current value when the accepted optimum $\check{r}^{PN(\alpha)}\left(\vec{V}^*\right)$ is more than $r^{PN(\alpha-1)}\left(\vec{V}^*\right)$.

In this work, the value of $\check{\delta}$ and $\hat{\delta}$ are chosen to be 3 and 1.02, respectively. More details about the optimization procedure can also be found in Peeters et al. [37,39].

4. Numerical results on a square plate with a cut-out

To demonstrate the performance of the strength optimization with the p-norm failure index, a representative application, namely a square plate with a circular cut-out under tension, is solved. A mesh refinement study is conducted to verify convergence of designs and a parametric analysis is carried out to test the effect of distinct values of p on the optimal results. The relative performance and efficiency of the globally-based p-norm method is quantified based on a comparative analysis with the locally-based min-max bound formulation.

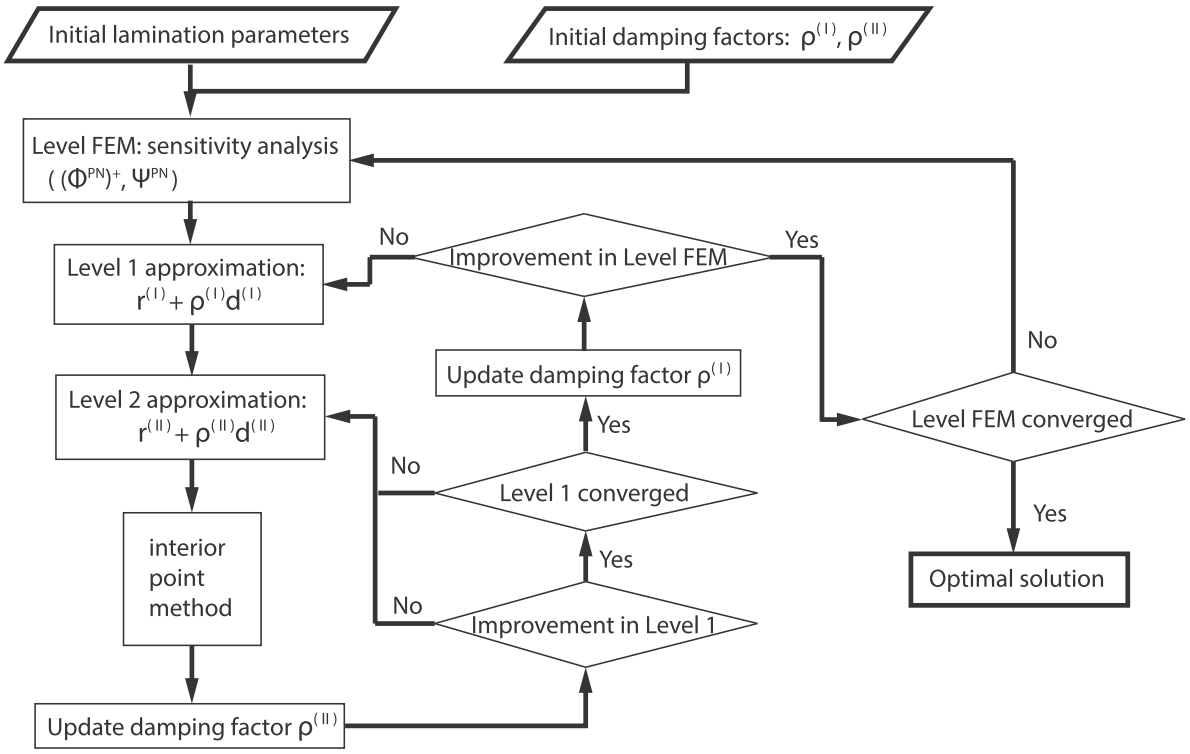

Fig. 2. Flowchart of the strength optimization for the VSLs.

In this model, the central points of the top and bottom edges in the plate are fixed in the x direction as shown in Fig. 3. The central points of the left and right edges are fixed in the y direction to prevent rigid body motion. Multipoint constraints are applied on both the left and right edges to ensure an identical deformation in the x direction. A point load of 500kN is applied on both the left and right edges. The material properties of the laminate are as follows: $E_1 = 148$GPa, $E_2 = 9.65$GPa, $G_{12} = 4.55$GPa and $\nu_{12} = 0.3$ (Nagy et al. [41]), with 1 indicating the fiber direction, 2 referring to the direction transverse to the fiber. The strength properties are chosen as those in Khani et al. [42]. The tension and compression strength along the fiber are $X^t = 2.28$GPa and $X^c = 1.44$GPa, respectively. The tension and compression strength transverse to the fiber are $Y^t = 0.057$GPa and $Y^c = 0.228$GPa, respectively. The pure shear strength is $S = 0.071$GPa.

The thickness of each ply is 0.6mm and the number of design layers is 6 in order to obtain a symmetric and balanced stacking sequence (i.e., 24 layers in total). The initial design is a quasi-isotropic laminate, where both $V_1, V_3 = 0$ at each design node. In order to have a broad view of the strength optimization with global failure index, the effect of the p value is studied systematically on a reference FEM model, a refined model and half of the reference model with symmetry boundary conditions.

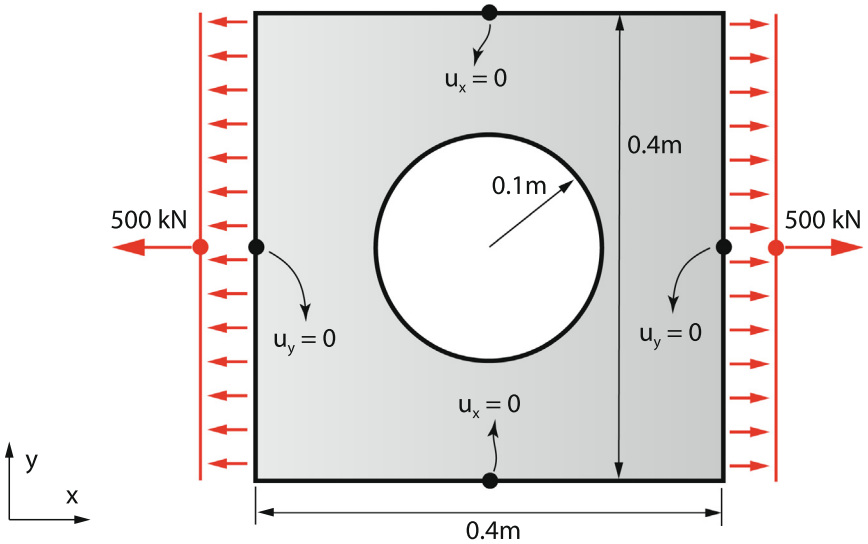

Fig. 3. Square plate with a cut-out in the center.

4.1. Effect of p on the optimal result

4.1.1. Numerical results in a reference model

In this test, the model is discretized using 512 elements and 576 design nodes, which also serves as a *reference* model in the subsequent sections. Observe that in this case no symmetry is used in the computation or the design process; instead, the entire plate is discretized to test how the design and analysis perform in the presence of two stress concentration regions at the top and bottom of the cut-out. The maximum local failure index associated with the initial design is $r_{max} = 1.033$, slightly over the allowable strength tolerance ($r = 1$). This intends to demonstrate that the maximum failure index in the model can be reduced to values below a critical material limit. The strength optimization with global failure index is conducted with $p = 1, 2, \cdots, 11$.

The distribution of the optimal $\vec{V}_1, \vec{V}_3$ and the corresponding local failure index (FI) are shown for four representative values of the power p ($p = 1, 4, 6, 8$) in Fig. 4. From the contour plots of the optimal local failure index, all the figures feature a stress concentration region in different sizes. This highly-stressed region is particularly visible with $p = 1$, which minimizes the volume average of the local failure indices. When the value of p increases, the stress concentration region reduces in size. This indicates that a higher p value, which elevates the effect of the critical local failure indices in the p-norm failure index, helps to reduce the maximum local failure index more effectively. In particular, for the results of $p = 6$, the maximum value is evenly spread towards its neighbours (from 0.346 to 0.2). However, when the value of p further increases to 8, the procedure appears to have less *local* control in the sense that the stress concentration reappears. The failure indices in the neighbourhood of the stress concentrations increase from 0.2 to roughly 0.3, which is undesirable. This indicates that care must be exercised when choosing the value of p since the procedure will generate an optimal value for all values tested, but has intrinsic numerical limitations for local control using large values of p.

For each case presented in Fig. 4, both optimal $\vec{V}_1$ and $\vec{V}_3$ in the top and bottom of the plate are close to 1. The associated fiber paths are aligned with the x direction in order to carry the tension in the model. When $p = 4$ or 6, this region is reshaped linking to the stress concentration region, resulting in a lower maximum failure index. Notably for the case $p = 6$, on the edges next to the stress concentration region, $\vec{V}_1$ is around -0.5 and $\vec{V}_3$ is approximately 0.5. This indicates that the fiber angles are oriented between 60° and 90° to transfer the internal force. As a result, the overall design results in an efficient reduction of the stress concentration. However, when $p = 8$, the contour plots of $\vec{V}_1$ and $\vec{V}_3$ exhibit fluctuations, which reflects limitations in *local* control as the nonlinearity of the objective function increases. The lamination parameters close to the top and bottom of the cut-out are around -0.5 for $\vec{V}_1$ and 0.6 for $\vec{V}_3$. The orientation of the corresponding fiber paths is around 70°, which reduces the tensile load carrying capacity in this section.

The convergence history of both the p-norm failure index and the associated maximum local failure index for $p = 1, 4, 6, 8$ is shown in Fig. 5. Regarding the p-norm failure index, the objective in the optimization, it converges within 8 accepted iterations (outer loop in the CCSA) for all the p values.

From the curves of the maximum local failure index, a reduction from 1.033 to at least 0.6 (a 42% improvement in strength) is achieved for all these cases. However, when $p = 6$ (Fig. 5 **(c)**), a slight increment appears for the maximum local index in the third accepted outer loop. In contrast, as $p = 8$, the history of the local failure index starts to fluctuate and the total number of iterations also increases to 8 (see Fig. 5 **(d)**). This behaviour is observed for $p = 10$ as well, where it takes 13 iterations to converge. The result is omitted here for brevity.

The fluctuation in the maximum local failure index is a drawback of using the p-norm failure index, as it does not precisely control the maximum local failure index with a finite p value. Thus, this may result in a slight increment of the maximum local value while the optimizer reduces the p-norm failure index. Fig. 5 **(d)** together with the contour plots for $p = 8$ in Fig. 4 indicate that numerical issues occur using a high value of p. This is due to the fact that while the p-norm failure index amplifies the effect of crucial local failure indices with a high value of p, the numerical noise in the numerical computation of the p-norm failure index and its sensitivity are amplified simultaneously. Also as discussed in the previous work [5,6,8,43], numerical instability and high nonlinearity occur as p increases over a certain range (which was found to be 6 in the work of Lee et al. [6]). Therefore, a proper p value should be chosen for the p-norm aggregation.

4.1.2. Numerical results in a refined model

In order to check the mesh dependency of the optimal solutions and the effect of mesh size on the proper value of p, the geometrical model is discretized with a refined mesh. In this *refined* model, there are 2048 elements and 2176 design nodes (nearly fourfold as those in the reference model). As in the previous test, the p values also range from 1 to 11. Fig. 6 illustrates the optimal results for $p = 1, 4, 6, 8$.

The optimal solutions in the refined model (Fig. 6) are compared with those in the reference model (Fig. 4). The main features in contour plots of $\vec{V}_1$ and $\vec{V}_3$ are identical between the two models for each listed p value. Specifically, $\vec{V}_1$ and $\vec{V}_3$ are close to 1 on the top and bottom of the plate. As the p value increases to 4 and 6, the red regions of $\vec{V}_1$ and $\vec{V}_3$ become sharper towards the central hole. Similar to the reference model for $p = 6$, the distributions of $\vec{V}_1$ and $\vec{V}_3$ next to the red regions around the cut-out appear to be approximately -0.5 and 0.5, respectively. When $p = 8$, the red regions in both $\vec{V}_1$ and $\vec{V}_3$ shift away from the central hole. Interestingly, in the optimum design of both the reference and the refined model, around 66% improvement for the maximum local failure index is achieved when $p = 6$, compared to the initial design. Hence, both quantitatively and qualitatively, the results confirm that the method developed in this work leads to reasonable mesh convergence in the optimal solutions.

The range in which the p value leads to good results using the refined model can be recognized from the contour plots of the optimal failure indices in Fig. 6. Similar to the results in the reference model, the maximum local failure index is effectively reduced for $p = 4, 6$ due to the power elevated in the p-norm failure index. Whereas, for $p = 8$, the local failure indices increase adversely again in the top and bottom half of the plate. Thus, despite the increase in the accuracy of the FEM analysis, the refinement of the mesh does not influence the maximum suitable value of p for the p-norm failure index.

4.1.3. Numerical results in half of the reference model

Both the reference model and the refined model are symmetric along the central line in x direction. Therefore, there are two locations that simultaneously obtain the maximum failure index. The presence of multiple local maxima could potentially affect the proper range of the p value in the p-norm failure index. The reason for analyzing a half model is to check whether a higher value of p can be used when there are no repetitive values in the aggregation. In view of this hypothesis, numerical results on the *half* model are created with symmetry boundary conditions imposed (i.e., move-

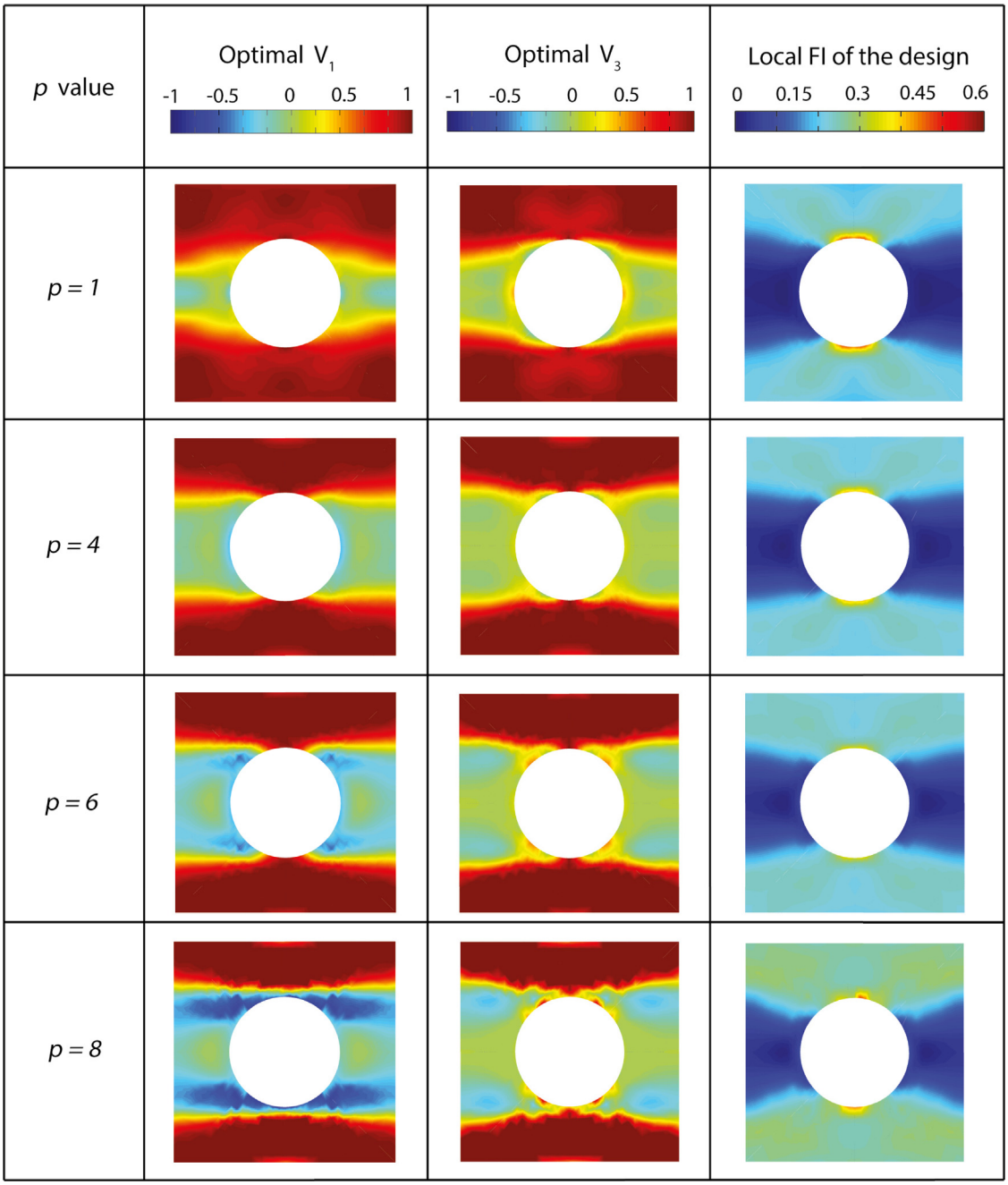

Fig. 4. Optimal $\mathbf{V}_1, \mathbf{V}_3$ and corresponding local failure indices of $p = 1, 4, 6, 8$ in the strength optimization using p-norm failure index in the reference model.

ment in y direction fixed to zero for the nodes on the symmetry axis).

The optimal results obtained in the half model are shown in Fig. 7. Compared to Fig. 4, it can be observed that the features of results for $p = 1, 4, 6$ in the half model are similar to those in the reference model. The local failure indices decrease as p increases from 1 to 6 and the red regions in $\vec{V}_1, \vec{V}_3$ are linking to the apex of the cut-out. However, the optimal lamination parameters of the two models for $p = 8$ are different. In particular, the result of the half model shows further improvement in terms of decreasing the maximum local failure index as shown in the fourth column of Fig. 7.

The convergence history of the four test cases is shown in Fig. 8. Similar to the tests with the reference model and the refined model, the curves for the p-norm failure index are initially decreasing monotonically. In terms of the maximum local failure index, convergence history for $p = 1, 4, 6$ is also similar to the previous models. Whereas, for $p = 8$ in the half model, even though the number of accepted iterations (i.e., the outer loop of the CCSA) increases to 18 (Fig. 5 (d)), the optimal local failure index obtained (0.314) is lower than that for $p = 6$ (0.345). This shows that the proper range of the p-value is affected by the structural details. From this figure, it seems the gap between the p-norm failure index and the maximum local failure index after each iteration under a certain p value is constant. We can not prove this from a mathematical point of view. However, it will be a valuable topic to proceed our work by exploring a sufficient calibration for the p-norm failure index similar to the works in [5,6,9].

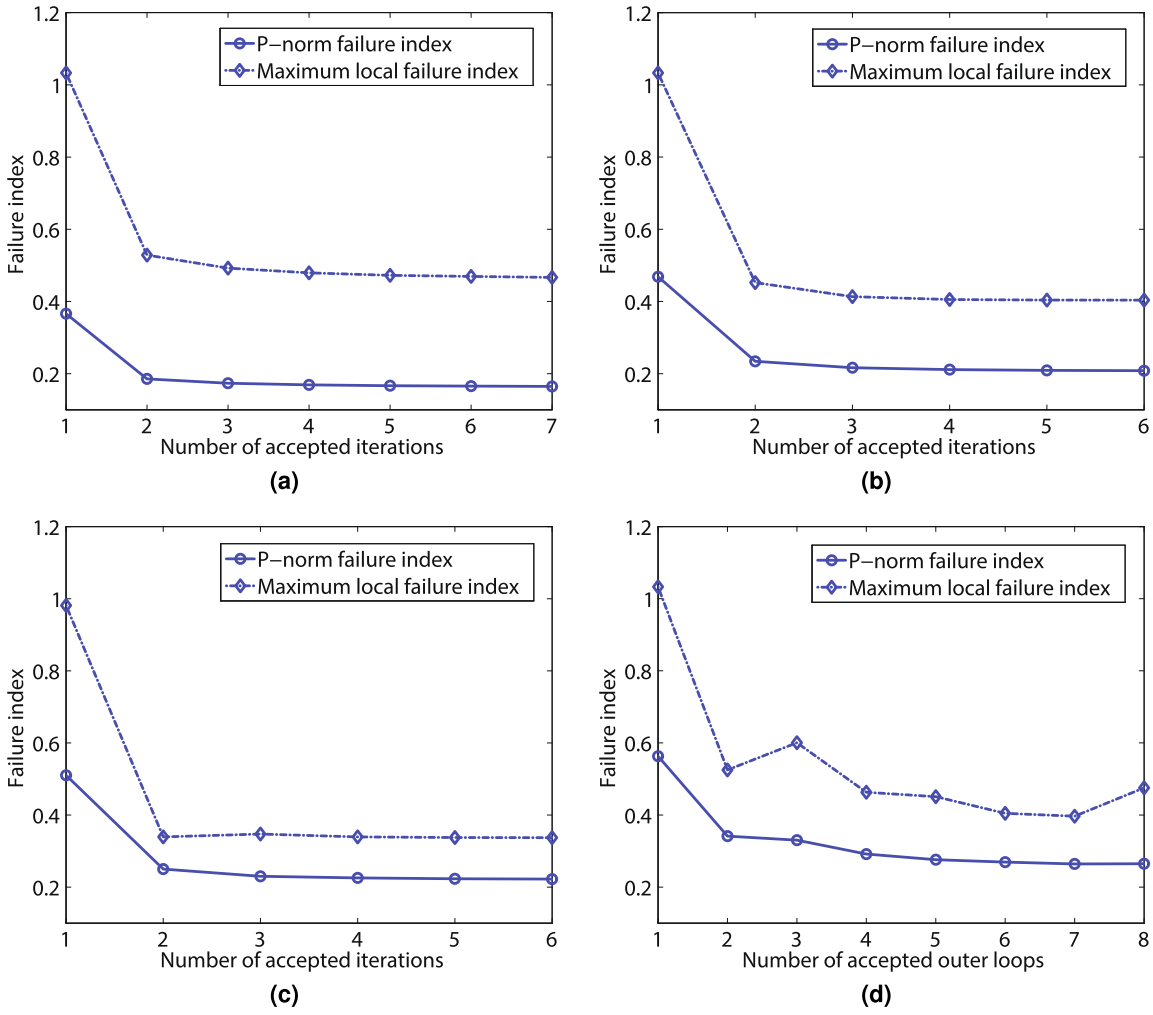

Fig. 5. History of the p-norm failure index with different p value and its associated maximum failure index in the iteration in the reference model **(a)** $p = 1$ **(b)** $p = 4$ **(c)** $p = 6$ **(d)** $p = 8$.

4.2. Optimal results with min-max bound formulation

In order to compare the performance of the proposed strength optimization using the p-norm failure index and the existing approach using local failure indices, the min-max bound formulation is implemented for the reference and refined model in this section.

The optimization problem is formulated as

$$\min_{\vec{V}_1,\vec{V}_3} \quad \beta \tag{35a}$$

$$\text{subject to} \quad r_i - \beta \leqslant 0, \tag{35b}$$

$$2V_{1,i}^2 - V_{3,i} - 1 \leqslant 0, \tag{35c}$$

$$V_{3,i} - 1 \leqslant 0 \qquad i = 1 \ldots n. \tag{35d}$$

The variable $\beta = \max\{r_{i(i=1\ldots n)}\}$ is the upper bound for the maximal local failure index in a structure. In essence, this formulation is a local version alternative to minimize $\|r_i\|_\infty$ (i.e., r^{PN} with $p \to \infty$) in Eq. (25). The results from min-max bound formulation are provided in Fig. 9.

From the local failure indices obtained in the design, the stress concentration in the model obviously disappears. The failure indices are more uniformly distributed in both the reference and the refined model. This is due to the fact that the maximal failure index in the optimization is precisely bounded by the parameter β in contrast to that in the p-norm failure index. From the optimal $\vec{V}_1$ and $\vec{V}_3$, it is obvious that the configuration of the red regions, crucial to reduce the stress concentration, converge to the case of $p = 6$ using the global approach (See Fig. 4 and 6). Thus, this confirms the optimum pattern to enhance the strength in this structure. The CPU time for the two test cases is also shown in Fig. 9.

The convergence history of the maximum local failure index obtained with the min-max bound formulation is shown in Fig. 10. From both sub-figures, this local measurement is reducing monotonically due to the precise bounding on $\max\{r_{i(i=1\ldots n)}\}$ (Eq. (35b)). In the reference model, an improvement of 74.4% is achieved in strength, with the maximum failure index dropping from 1.033 to 0.264. Obviously, this is more effective compared to using the p-norm failure index. Also, in the refined model, the maximum local failure index decreases from 1.083 to 0.291, achieving a 73.1% improvement. In both sub-figures, the p-norm failure index corresponding to $p = 6$ obtained in each iteration is also plotted with the dashed lines as a qualitative reference. With the min-max bound formulation, the p-norm failure index is not decreasing monotonically. This is due to the fact that a large number of failure indices reach the upper bound in the optimal design, yielding a slight increase in the p-norm failure index towards the end of the history.

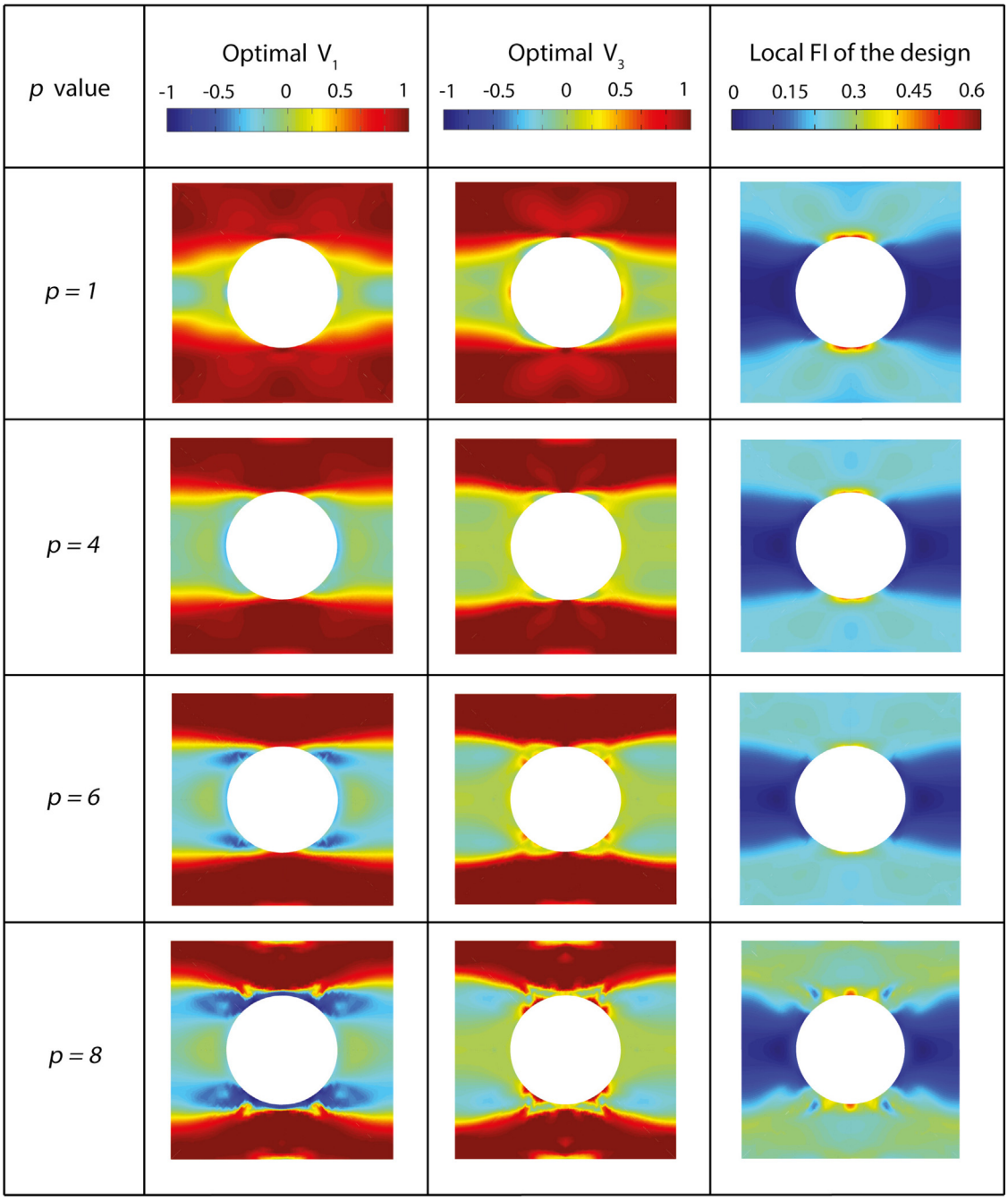

Fig. 6. Optimal $\vec{V}_1, \vec{V}_3$ and corresponding local failure indices of $p = 1, 4, 6, 8$ in the strength optimization using p-norm failure index in the refined model.

4.3. Comparative analysis for strength optimization using the p-norm failure index and min-max bound formulation

To assess the overall performance of the strength optimization using the global and local failure indices, the data of the maximum local failure index and the corresponding CPU time in the three aforementioned models is shown in Fig. 11. According to Fig. 11 (a), the trends for the reference and the half models are the same since the models are essentially identical. The curve of the maximum local failure index for the refined model is higher, due to the higher stress concentration in the FEM model. In the refined model, the maximum local failure index reaches a minimum when $p = 6$. Thereafter, it starts to fluctuate when p increases further. The curve for the reference model reduces to the minimum when $p = 7$. In contrast, for the half model, the curve keeps decreasing until $p = 9$. Combining the results from Section 4.1.1–4.1.3, the maximum value of p that can be used in practice varies between 6 and 9, depending on the structural details.

In Fig. 11 (a), the result from the min-max bound formulation is included to give a qualitative comparison. The value from the reference model is 0.264, which is even 15.4% lower than 0.312 obtained from the best case with p-norm failure index in the half model. Correspondingly, the value achieved in the refined model is 0.291, approximately 20.7% lower than 0.367 in the same model with p-norm failure index of $p = 6$. Therefore, the min-max bound formulation performs significantly better than the p-norm failure index in enhancing the strength of the VSLs.

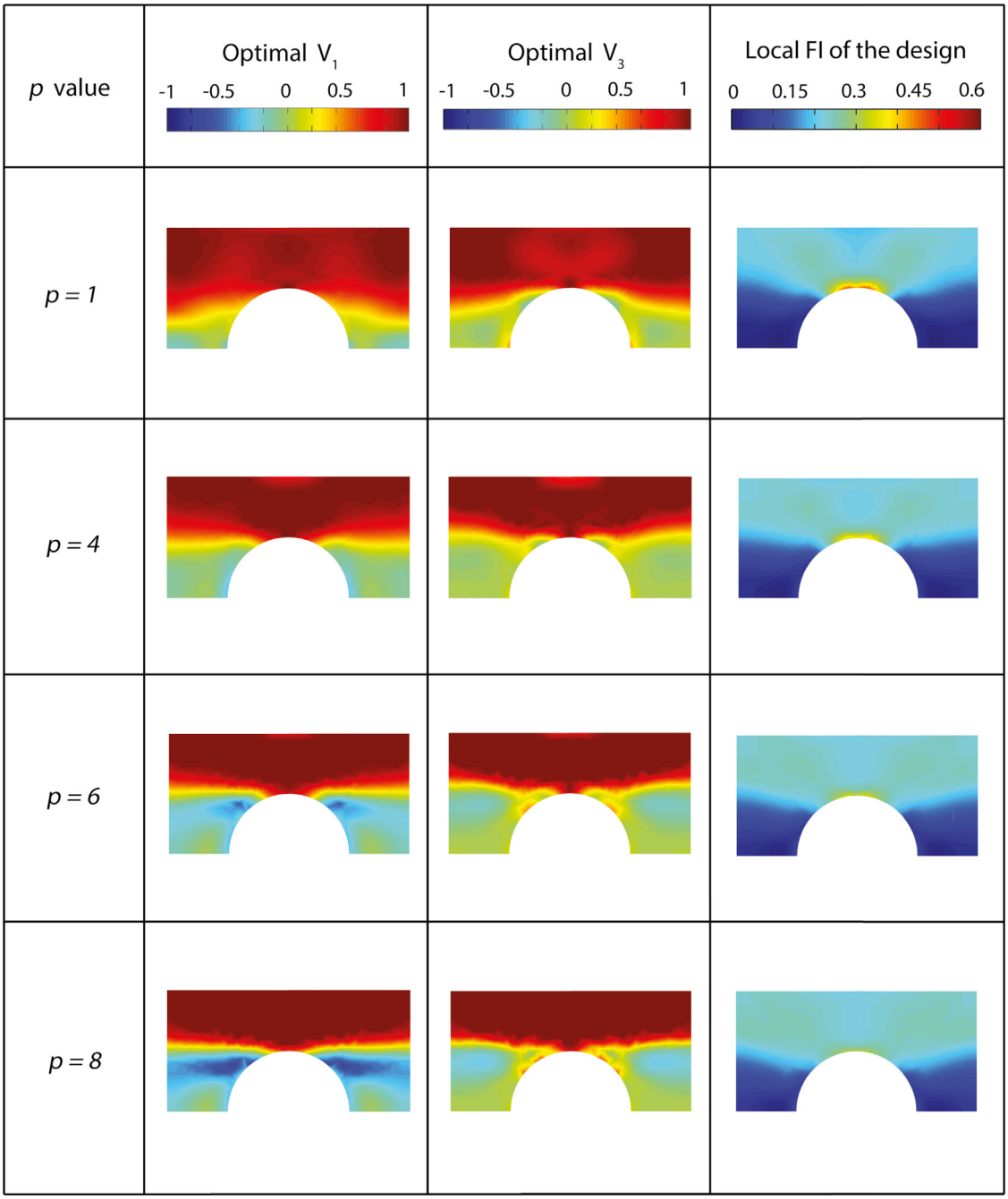

Fig. 7. Optimal $\vec{V}_1, \vec{V}_3$ and corresponding local failure indices of $p = 1, 4, 6, 8$ in the strength optimization using p-norm failure index in the half model.

The result in a comparative work by Izzi et al. [17] shows some common features for the layout of the optimal design from both works: 1) The carbon fibers on the top of the plate align with the horizontal direction to bear the tension. Whereas the fibers around the central hole steer around the cut-out to transfer the shear. 2) The highest failure load is located on the top edge of the central hole in the reference model. However, this disappears after the optimization in both works. The stress becomes evenly distributed in this region.

Regarding the difference of the numerical results between these two approaches, we reduce the feasible domain to Eq.(4) as we described. In contrast, the authors in [17] use the polar parameters in the first step of their method, where the feasible domain spans the entire feasible design space without any assumption on the lay-ups of the laminates. It is equivalent to Eq.(3), which is wider than ours. Thus, the solution they obtained can be better in this phase.

It is interesting to note that a high value of p ($p = 709$) can be utilized in their framework. This renders them to achieve an equivalent solution using the min-max bound formulation. We think the reason can be as follows. The work by Izzi et al. [17] uses a general sequential least square quadratic programming (SLSQP) to solve the optimization. With this iterative approach, the optimizer still manages to reach an optimum despite a high value of p. Details associated with the SLSQP can be found in [44]. However, in our approach or those using the method of moving asymptotes (MMA) in topology optimization, the optimization is solved using the interior point method. The sub-problem with a high value of

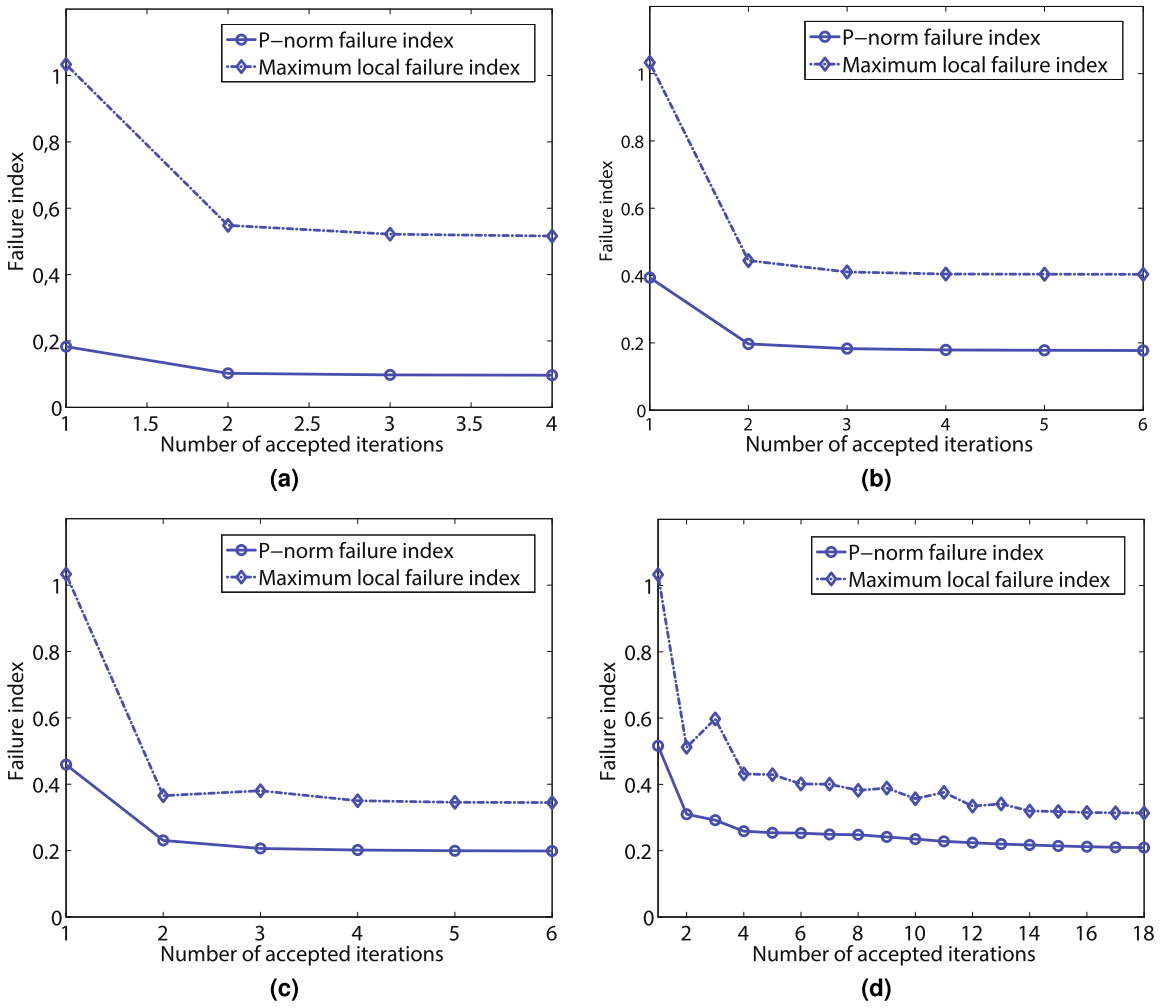

Fig. 8. History of the p-norm failure index with different p value and its associated maximum failure index in the iteration in the half model **(a)** $p = 1$ **(b)** $p = 4$ **(c)** $p = 6$ **(d)** $p = 8$.

p in the p-norm failure index leads to solutions that are fluctuating, which is difficult to converge. Later, we found this can possibly be alleviated by increasing p gradually during the iterations [45].

Since the SLSQP converges with a large p value, and the sensitivity of the p-norm failure index is efficient to obtain using the adjoint method, it can be a good idea to solve the aggregated strength optimization with the SLSQP formulation.

From Fig. 11 (b), the curves for the p-norm failure index show that the CPU time is not sensitive to p as it changes from 1 to 6. In the reference model, the CPU time is constant at around 800s. The values are about 200s and 8500s in the half model and the refined model, respectively. The increment of the computational cost is close to quadratic with respect to the size of the problem (the number of design variables). This is due to the fact that the computational cost is dominated by the computational complexity to resolve the Schur Complement in the interior point method with the direct method. When the value of p is higher than 6, the computational cost starts to increase. This is because the number of inner loops taken within every outer loop increases evidently in the CCSA due to the numerical instability and the non-linearity of the p-norm function.

In contrast to the p-norm failure index, the computational cost of the min-max bound formulation is indeed heavy. Its CPU time for the reference model is 14950s, almost ten-fold of 1512s with $p = 7$ using p-norm failure index. The CPU time for the refined model is 812070s, more than 70 times of that from p-norm failure index with $p = 6$ (10908s) due to the quadratic increment of the computational work.

The gaps between the maximum local failure index ($\|r\|_\infty$) and $\|r\|_p$ ($p = 1, 2, \cdots, 11$) obtained using the p-norm failure index in all of the three test models are presented in Fig. 12. All the three sub-figures show that the gap decreases consistently when the p value increases within a region, referred to as the well-conditioned range. With a higher value of p beyond this range, the gap between the two values fluctuates due to the numerical issues induced. Therefore, the highest p value in this well-conditioned range should opt for the p-norm failure index. In this case, the optimum p value is 6, the most conservative range among all these cases. In addition, we find in this numerical case that a higher p value can be chosen by removing the symmetric part in the half model. As shown in Fig. 11 and Fig. 12, the maximum failure index can be reduced further with a lower CPU time cost as the model size is halved.

According to the comparative analysis, the min-max bound formulation is more effective than the p-norm failure index in improving the strength of the VSLs. However, its computational cost is obviously more demanding, especially for large scale problems. Therefore, to achieve a good compromise between the

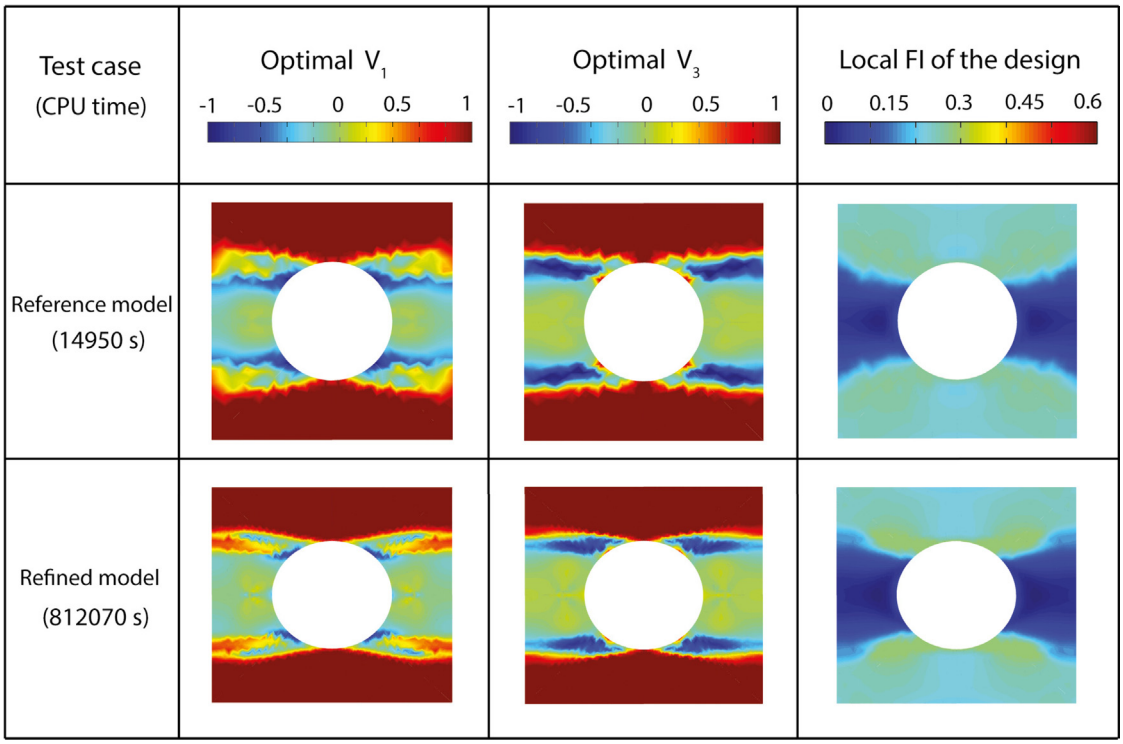

Fig. 9. Optimal $\vec{V}_1, \vec{V}_3$ and corresponding local failure indices in the strength optimization using min-max bound formulation.

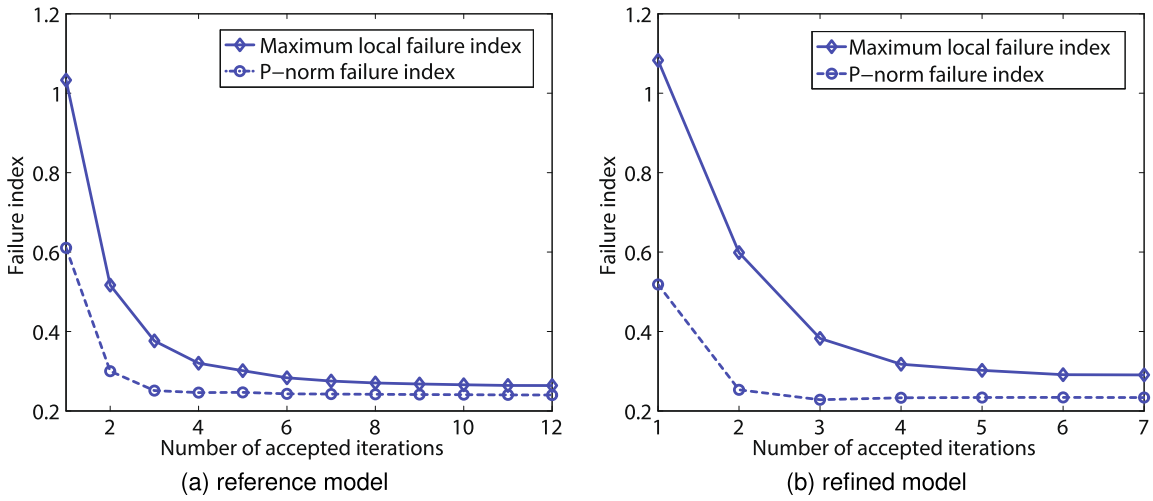

Fig. 10. History of the maximum local failure index using the min-max bound formulation and its associated p-norm failure index in the iteration ($p = 6$).

strength improvement and the computational effort, the well-posed p-norm failure index is recommended for the strength optimization of the VSLs.

5. Strength optimization on the L-shaped plate

The second numerical study is implemented on the L-shaped plate (See Fig. 13), which is a challenging problem due to the stress singularity at the reentrant corner. The intention of this study is to exploit the performance of the proposed method under such an extreme condition. The boundary conditions of the model are as follows: the top edge of the plate is fixed and a shear load of 500kN/m is applied on the lower half of the right edge. The parameters associated with the variable stiffness laminate are the same as those in the previous example. The initial layout is again chosen to be a quasi-isotropic laminate.

5.1. Mesh-convergence study

In the mesh-convergence study, the numerical model is first discretized with 8 elements for the 0.4m edge, and 12 elements for the 0.6m edge. Subsequently, it is refined using $12 \times 18, 16 \times 24$ and 20×30 elements for the two edges, respectively. From the previous test case, the best design is achieved with $p = 6$ in the p-norm failure index. Therefore, the optimal results for $p = 6$ in each mesh level are plotted in Fig. 14. The distributions of $\vec{V}_1$ and $\vec{V}_3$ converge to a unique solution as the mesh is refined. The distributions of the local failure indices also exhibit mesh

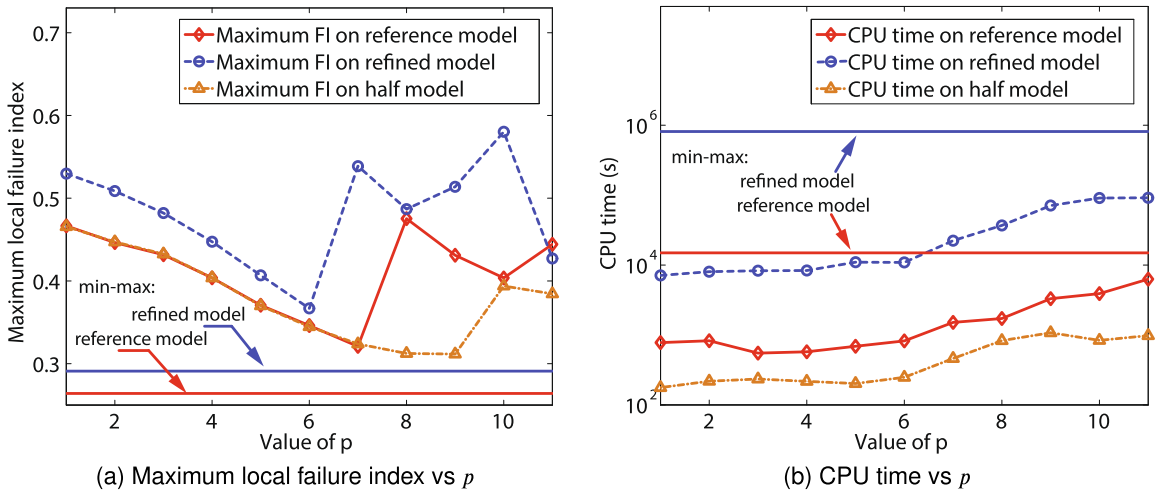

Fig. 11. Comparison of the maximum local failure index and CPU time cost for various p values in the reference model, refined model and the half model using p-norm failure index and min-max bound formulation.

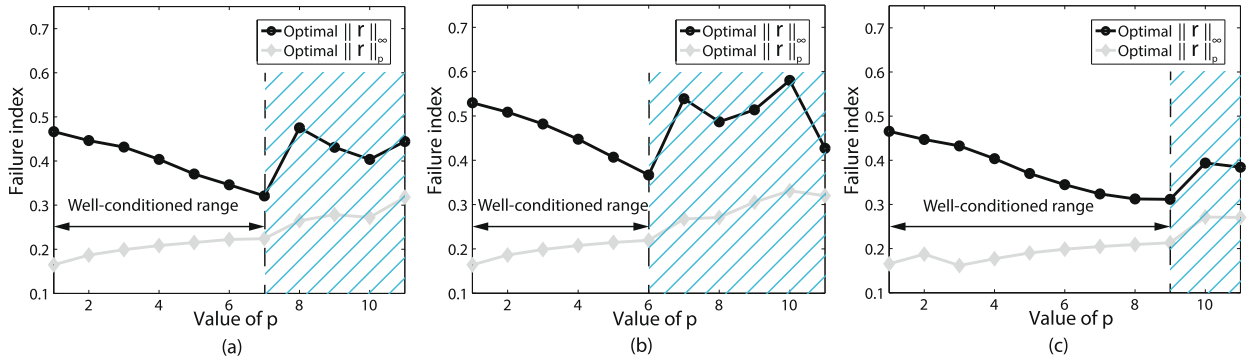

Fig. 12. Gaps of optimal $\|r\|_\infty$ vs $\|r\|_p$ in three different models (a) the reference model, (b) the refined model, (c) the half model.

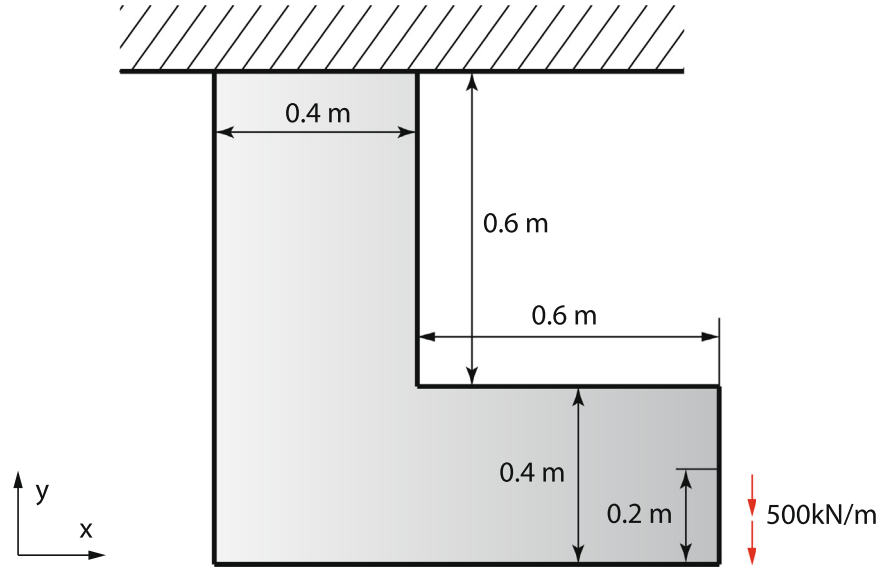

Fig. 13. L-shaped plate.

convergence. Some discrepancy exists in the lamination parameters, presumably due to the fact that stress singularity already induces some numerical instability when $p = 6$ in this case. To verify the mesh convergence, the same tests for $p = 1, 4$ are conducted. The corresponding results of different sizes in the mesh refinement converge to a unique solution. The figures are omitted here for brevity.

The effect of different p values on the optimal solution is also investigated for this case. The results of the 20×30 mesh for $p = 1, 4, 6$ are shown in Fig. 15. From the contour plots of local

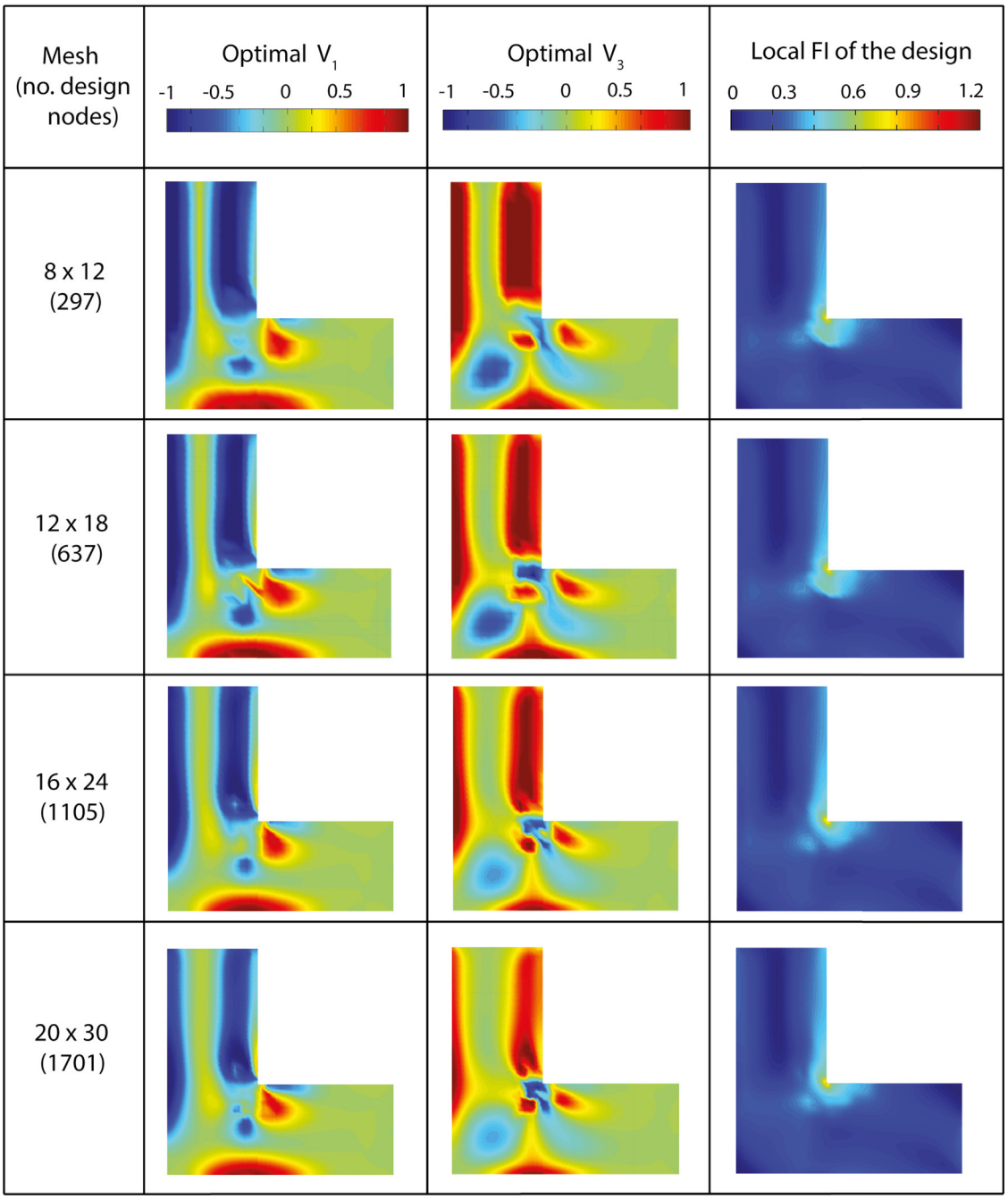

Fig. 14. Study of the mesh convergence of $\vec{V}_1, \vec{V}_3$ and corresponding local failure indices using p-norm failure index ($p = 6$).

failure indices, it can be observed that the maximum local failure index reduces as the value of p increases. Simultaneously, a larger portion of the structure contributes to the load carrying capacity around the corner. This again confirms that a high value of p in the well-conditioned range effectively relieves the stress concentration.

As the p value increases, the distribution of the optimal $\vec{V}_1$ and $\vec{V}_3$ also adapts to reduce the maximum local failure index. When the value of $p = 1$ changes to $p = 4, 6$, the $\vec{V}_3$ at the reentrant corner turns from 0 to -1. Together with $\vec{V}_1$ being around 0, this indicates that the fiber angles should be roughly $[\pm 45^\circ]_s$ with respect to the x axis to alleviate the stress concentration. Simultaneously, the pair of $\vec{V}_1$ and $\vec{V}_3$ at the bottom left of the plate also changes from 0 and -0.7, to 0 and -0.4 gradually to dissipate the internal load. The corresponding layout of the laminate on the bottom right part of the plate becomes quasi-isotropic for $p = 6$ (both the $\vec{V}_1$ and $\vec{V}_3$ are close to 0) in order to carry the shear load on the edge. As a result, the maximum failure index in these cases is obviously lower than that of $p = 1$.

The main conclusion of the mesh-convergence study is that the proposed method basically generates mesh-independent solutions even in a model with stress singularity. However, it is worth noting that numerical problems already appear when $p = 6$ in this case.

5.2. The optimal design from the min-max bound formulation

The optimal designs obtained using the min-max bound formulation for different mesh sizes are presented in Fig. 16. As the mesh

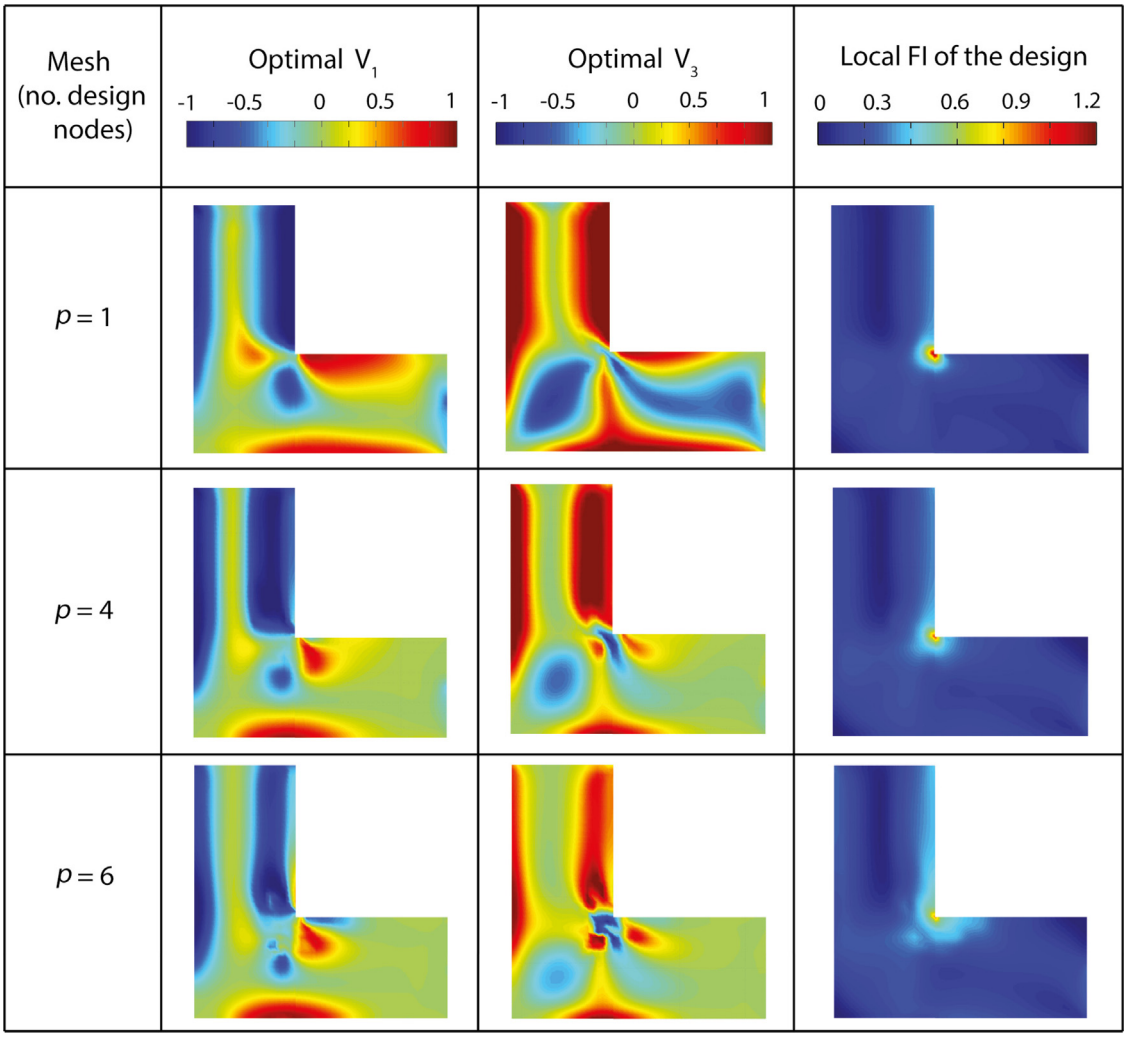

Fig. 15. Investigation of different p values on the optimal solution using p-norm failure index for 20×30 mesh.

becomes denser, the broad features of the optimal designs resemble the optimal designs obtained from the p-norm (comparing Fig. 16 to Fig. 14). However, some local discrepancies between results with different mesh sizes can be apparently observed. This can be interpreted by the numerical problem from minimizing the maximum failure index precisely with stress singularity occurrence at the reentrant corner, which perturbs the optimizer in the iterations.

From the contour plots of the local failure indices in Fig. 16, the maximum local failure index obtained for each mesh level is lower than that from the p-norm failure index. Simultaneously, the unique upper bound in the min-max bound formulation results in a larger portion of the plate contributing to the load carrying capacity (i.e., larger light blue region but lower maximum local failure index).

5.3. Comparative analysis of the optimal results from the p-norm failure index and min-max bound formulation

In this section, the maximum local failure index and the CPU time cost obtained from the strength optimization of using the p-norm failure index and the min-max bound formulation are depicted in Fig. 17.

The maximum local failure indices obtained with the four meshes investigated before are shown in Fig. 17 (a). The value for the initial quasi-isotropic laminate increases from 0.856 to 1.336 as the mesh is refined because of the singularity issue. For the results of each mesh level using p-norm failure index, a higher p value results in a more effective reduction in the maximum local failure index. With only one exception for $p = 10$ with 637 design nodes, which overlaps with that of $p = 8$ due to the occurrence of numerical noise. Consistent with the previous test case, the min-max bound formulation generates a lower failure index compared to the p-norm formulation. The remark of the results from the p-norm failure index and the min-max bound formulation in this figure is two-fold: first, the min-max bound formulation is superior in strength enhancement of the VSLs; second, the p-norm formulation provides a converged design even with stress singularity given a proper p value.

The CPU time using the p-norm failure index and the min-max bound formulation is presented in Fig. 17 (b). The curve for $p = 6$ represents the relatively well-conditioned case, whereas $p = 10$ represents the case with a numerical issue. The slope of all these curves is roughly quadratic, identical to the conclusion in the square plate with a cut-out case. Apparently, the data for $p = 6$ in the model with 1105 and 1701 design nodes is approaching that for $p = 10$, complying with the assumption that numerical issues already appear as presented in Fig. 14. As the upper bound β in the min-max formulation shown in Eq.(35) controls the maximum local failure index more precisely, and due to the numerical disturbance from strength singularity as the mesh refined further, the min-max formulation reaches the stopping criterion with fewer

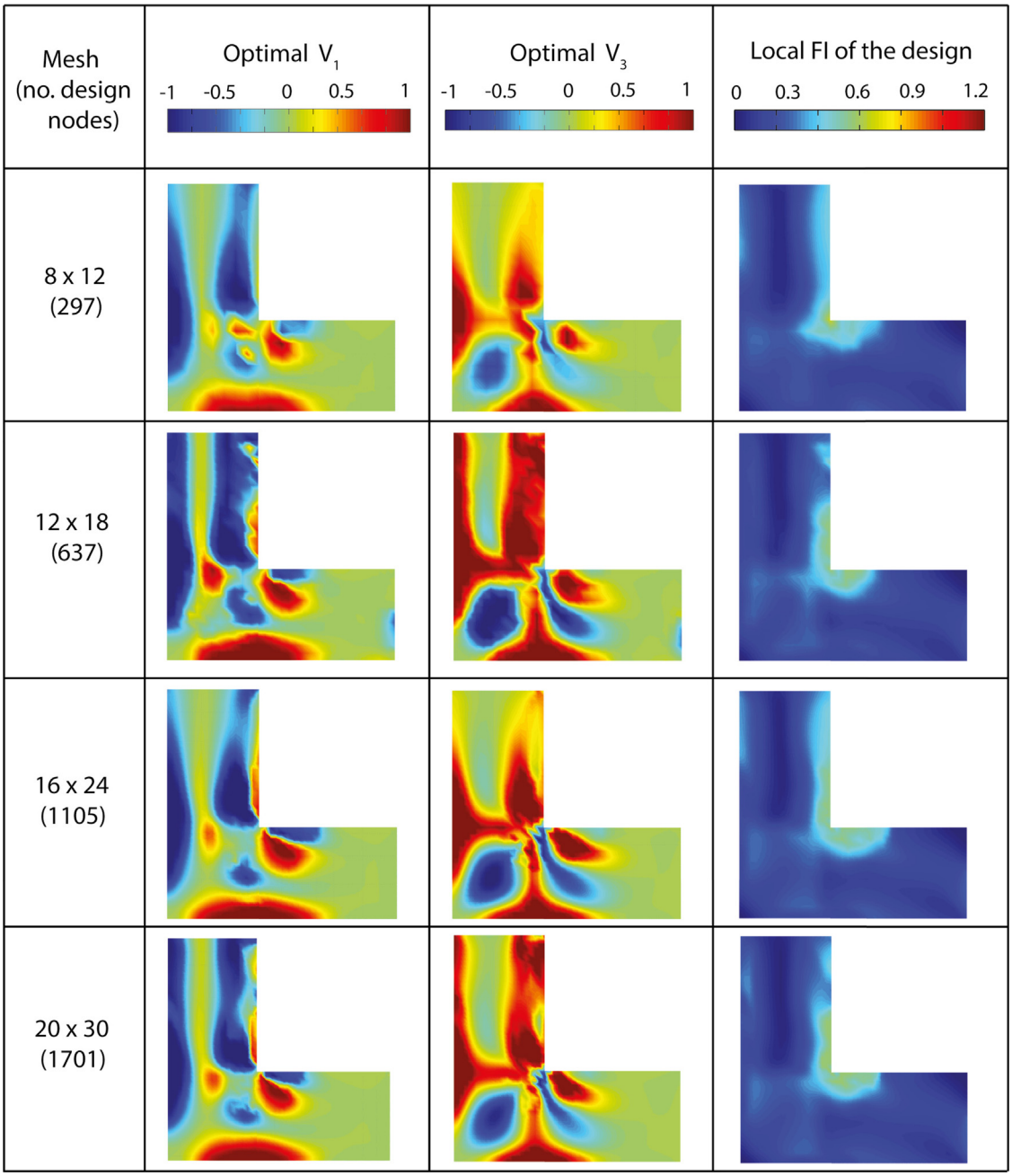

Fig. 16. Study of the mesh convergence of $\vec{V}_1, \vec{V}_3$ and corresponding local failure indices using local min-max formulation.

iterations. This bends the curve for the CPU time of the min-max formulation to be closer to those using the p-norm failure index as the mesh is refined to 1105 and 1701 nodes in Fig. 17 (b). However, its maximum local failure index is not fully reduced yet for the 1701 nodes (20×30 elements) model as can be seen in Fig. 17 (a). Regarding the min-max bound formulation, the computational cost is one order of magnitude higher than the inferior case of $p = 10$ in the log-log plot.

Eventually, the optimal designs obtained from the p-norm failure index and the min-max bound formulation are briefly compared to show the differences. The difference of the optimal $\vec{V}_1$ and $\vec{V}_3$ obtained from the p-norm failure index ($p = 6$) and the min-max formulation under the 8×12 mesh are shown in Fig. 18 in Appendix B. From Fig. 18 (a) and (b), it can be deduced that the most obvious difference locates on the top left part and the part next to the corner for both $\vec{V}_1$ and $\vec{V}_3$. The other parts match for $\vec{V}_1$ obtained from both methods, the $\vec{V}_3$ distribution is similar as well. Interestingly, the contour plot showing the difference in failure index (Fig. 18 (c)) indicates that the difference of the highest local failure index (around the corner of the L shaped plate) is small. The most obvious difference of the failure index locates only on the left top part and the part around the corner. This shows that the p-norm failure index helps to reduce the maximum local failure index effectively in this case.

In order to have a view on the performance of the proposed strength optimization approach using the p-norm failure index on general structures without singularity or hole, we recommend executing the approach on a cantilever plate or a three point bend-

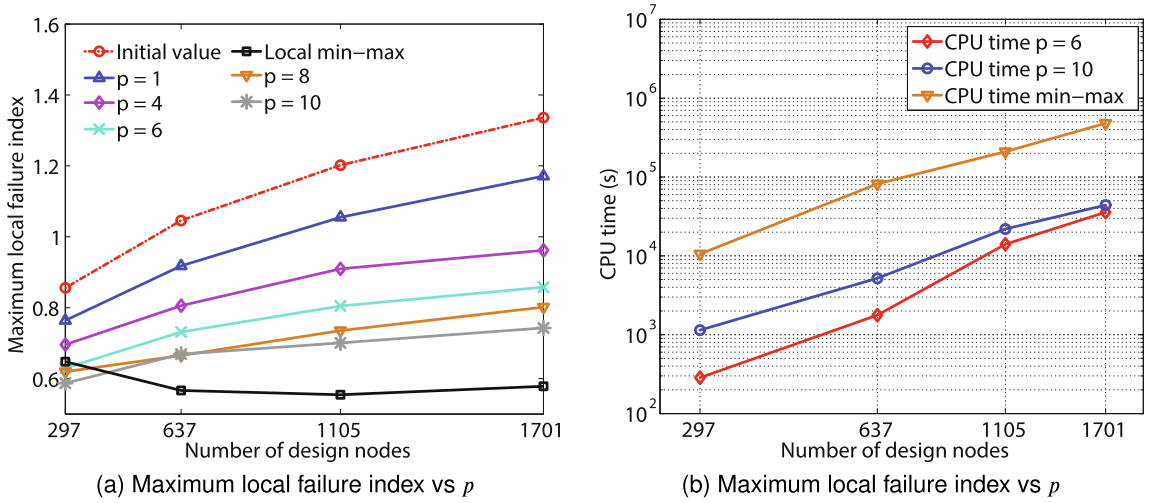

Fig. 17. (a) the maximum local failure index for the optimum design of $p = 1, 4, 6, 8, 10$ in the p-norm failure index and the min-max bound formulation, (b) log-log plot of the CPU time cost for $p = 6, 10$ and the min-max bound formulation.

ing plate without symmetry. Most likely, on the structures without either symmetry or singularity, a higher p value (base on our test in Section 4.1.3) can be employed in the p-norm failure index to further improve the performance of the approach.

6. Conclusion

In the current work, the p-norm formulation is applied to enhance the computational efficiency of strength optimization for VSLs. Due to the intrinsic aggregation of the p-norm formulation, the size of the subsequent optimization problems can be significantly reduced. Therefore, the computational work to address the Schur complement of the sub-problem, which dominates the overall cost, is effectively reduced. The sensitivity analysis of the p-norm failure index also becomes efficient using the adjoint method. Additionally, an elliptical formulation of the conservative failure envelope is employed to fit the Tsai-Wu failure criterion in the lamination parameter space. This general approach can also be used in conjunction with other failure criteria. Based on this formulation, a convex two-level approximation is derived for the p-norm failure index.

The proposed method in this work leads to a stable convergence in the iterative optimization procedure and mesh-independent optimal results. In the numerical test of a square plate with a cut-out, the effect of the p value on the optimal results is studied on a reference model, a refined model and a half model. A minimum of 42% improvement in strength is achieved against the initial quasi-isotropic laminate. The optimal lamination parameters exhibit mesh convergence expected using the proposed hybrid interpolation method. By comparing the optimal solution from the local min-max bound formulation, the computational cost is reduced dramatically using the global aggregation method with a proper p value, albeit the maximum local failure index obtained is relatively higher.

In the L-shaped case, the numerical results illustrate that the computational cost can be reduced by at least an order of magnitude using this method compared to the local min-max formulation even in the presence of a stress singularity. A p value higher than 6 still reduces the maximum local failure index considerably, however, some numerical instabilities already have an effect on the iterative procedure.

In future work, we can attempt the approach under multiple load cases, which guarantees that the structures withstand different operating conditions. This will contribute to generate practical engineering designs.

Declaration of Competing Interest

The authors declare that they have no known competing financial interests or personal relationships that could have appeared to influence the work reported in this paper.

Acknowledgements

Zhi Hong would like to thank the financial support from the China Scholarship Council CSC (No. 201406020095) for this research. Yujie Guo would like to thank the National Natural Science Foundation of China (Grant no. 11972187) for their support.

Appendix A. Sensitivity analysis for the linear expansion and load redistribution part of $r^{PN(I)}$

The coefficient matrices $\mathbf{\Phi}^{PN}$ in Eq. (17) is a function of $\mathbf{\Phi}_g$ (Eq. (11)), which is obtained from the internal force $\vec{N}_g$. Thus, the complete sensitivity analysis of r^{PN} should account for the linear expansion and the load redistribution effect due to the change of $\mathbf{A}$ in $\mathbf{\Phi}^{PN}$. According to the chain rule, the derivative of r^{PN} with respect to $\mathbf{A}_j$ can be written as

$$\frac{\partial r^{PN}}{\partial \mathbf{A}_j} = \sum_{i=1}^{n} \frac{\partial r^{PN}}{\partial r_i} \left(\sum_{g=1}^{n_g} \frac{\partial r_i}{\partial r_g} \frac{\partial r_g}{\partial \mathbf{A}_j} \right). \tag{36}$$

Substituting Eq. (12) into Eq. (11), the derivative of r_g with respect to $\mathbf{A}_j$ can be obtained:

$$\frac{\partial r_g}{\partial \mathbf{A}_j} = \frac{1}{2} \frac{\partial \left(\vec{N}_g \vec{q}_g^T + \vec{q}_g \vec{N}_g^T \right) : \mathbf{A}_g^{-1}}{\partial \mathbf{A}_j}. \tag{37}$$

Rearranging the terms, it becomes:

$$\frac{\partial r_g}{\partial \mathbf{A}_j} = \frac{1}{2} \frac{\partial \left(\vec{q}_g^T \left(\mathbf{A}_g^{-1} \right)^T \vec{N}_g + \vec{N}_g^T \left(\mathbf{A}_g^{-1} \right)^T \vec{q}_g \right)}{\partial \mathbf{A}_j}. \tag{38}$$

The chain rule is required again to implement this calculation, which is given by

$$\frac{\partial r_g}{\partial \mathbf{A}_j} = \sum_{g=1}^{n_g} \frac{\partial r_g}{\partial \mathbf{A}_g^{-1}} \frac{\partial \mathbf{A}_g^{-1}}{\partial \mathbf{A}_j}, \tag{39}$$

and the derivative of a matrix inverse can be obtained by

$$\frac{\partial r_g}{\partial \mathbf{A}_g^{-1}} = -\mathbf{A}_g \frac{\partial r_g}{\partial \mathbf{A}_g} \mathbf{A}_g. \tag{40}$$

The derivative of $\vec{N}_g$ with respect to $\mathbf{A}_g$ in r_g of Eq. (40) yields the linear part and load redistribution part in the sensitivity that are being discussed in this section:

$$\frac{\partial \vec{N}_g}{\partial \mathbf{A}_g} = \vec{e}_g + \mathbf{A}_g \frac{\partial \vec{e}_g}{\partial \mathbf{A}_g}, \tag{41}$$

where $\vec{e}_g$ is the strain at the Gauss point.

The derivative of the strain in the second part is

$$\frac{\partial \vec{e}_g}{\partial \mathbf{A}_g} = \mathbf{B}_g \frac{\partial \vec{u}_e}{\partial \mathbf{A}_g}, \tag{42}$$

where $\mathbf{B}_g$ is the strain-displacement matrix, and $\vec{u}_e$ is the displacement in the e^{th} element. The adjoint method is needed to estimate the load redistribution effect. Taking the derivative of Eq. (6) with respect to $\mathbf{A}_g$, the derivative of the displacement is obtained by

$$\frac{\partial \vec{u}}{\partial \mathbf{A}_g} = -\mathbf{K}^{-1} \frac{\partial \mathbf{K}}{\partial \mathbf{A}_g} \vec{u}. \tag{43}$$

Substituting Eqs. (42), (43) back into Eq. (41) and then putting the result into $\frac{\partial r_g}{\partial \mathbf{A}_g}$, the pseudo load for the adjoint problem in the r_g level is ($\mathbf{A}_g$ is symmetric)

$$\vec{t}_g = \mathbf{B}_g^T \mathbf{A}_g^T \mathbf{A}_g^{-1} \vec{q}_g = \mathbf{B}_g^T \vec{q}_g. \tag{44}$$

Finally, substituting the result obtained in Eq. (38) (based on Eqs. (39)–(44)) back into Eq. (36), the linear part of the sensitivity for the p-norm failure index is

$$\left.\frac{\partial r^{PN}}{\partial \mathbf{A}_j}\right|_l = \sum_{i=1}^{n} a_i \sum_{g=1}^{n_g} b_{i,g} \mathbf{A}_j^{-1} \left(\mathbf{A}_g \frac{R_{j,g}}{2} \left(\vec{q}_g^T \mathbf{A}_g^{-1} \vec{e}_g + \vec{e}_g^T \mathbf{A}_g^{-1} \vec{q}_g \right) \mathbf{A}_g \right) \mathbf{A}_j^{-1}. \tag{45}$$

The adjoint part of the sensitivity for the p-norm failure index is

$$\left.\frac{\partial r^{PN}}{\partial \mathbf{A}_j}\right|_{adj} = -\vec{v}^T \left(\sum_{g=1}^{n_g} \mathbf{A}_j^{-1} R_{j,g} \left(\mathbf{A}_g \cdot \frac{\partial \mathbf{K}}{\partial \mathbf{A}_g} \cdot \mathbf{A}_g \right) \mathbf{A}_j^{-1} \right) \vec{u}, \tag{46}$$

where $a_i = \frac{\partial r^{PN}}{\partial r_i}$ is the i^{th} coefficient of $\mathbf{\Phi}_{i,j}$ in Eq. (19), and $b_{i,g} = \frac{\partial r_i}{\partial r_g}$ is the g^{th} coefficient of $\left(\mathbf{\Phi}_g : \mathbf{A}_g^{-1} \right)$ in Eq. (13). The adjoint vector $\vec{v}$ is obtained from

$$\mathbf{K}\vec{v} = \vec{t}, \tag{47}$$

where the pseudo load $\vec{t}$ is

$$\vec{t} = \sum_{i=1}^{n} a_i \sum_{g=1}^{n_g} b_{i,g} \vec{t}_g. \tag{48}$$

It is important to note that caution needs to be executed when implementing $\frac{\partial \mathbf{K}}{\partial \mathbf{A}_g}$, since the result is a three-dimensional matrix. The calculation is executed component-wise from the derivative of $\mathbf{K}_g$ (stiffness matrix at the g^{th} Gauss point) with respect to the terms in $\mathbf{A}_g$. Also keep in mind that $\mathbf{A}_g$ is a symmetric matrix. Details are omitted here for the sake of brevity.

Appendix B. Absolute differences of the optimal design between using the *p*-norm failure index and the min-max formulation

Fig. 18

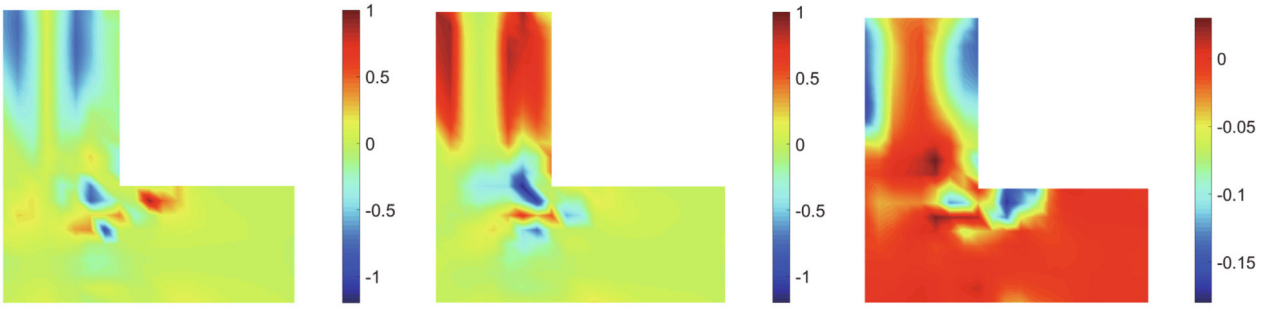

(a) Absolute differences of optimal V_1 (b) Absolute differences of optimal V_3 (c) Absolute differences of local FI

Fig. 18. Absolute differences of the optimal $\vec{V}_1, \vec{V}_3$ and the corresponding local failure index between using the p-norm aggregation ($p = 6$) and those using the min-max formulation (value of the p-norm subtracts those from the min-max formulation).

References

[1] Khani A, IJsselmuiden ST, Abdalla MM, Gürdal Z. Design of variable stiffness panels for maximum strength using lamination parameters. Compos Part B: Eng 2011;42(3):546–552. doi: 10.1016/j.compositesb.2010.11.005. ISSN 1359-8368. http://www.sciencedirect.com/science/article/pii/S1359836810002131.

[2] Duysinx Pierre, Sigmund Ole. New developments in handling stress constraints in optimal material distribution. In: 7th AIAA/USAF/NASA/ISSMO Symposium on Multidisciplinary Analysis and Optimization, page 4906; 1998. doi: https://doi.org/10.2514/6.1998-4906.

[3] Holmberg Erik, Torstenfelt Bo, Klarbring Anders. Stress constrained topology optimization. Struct Multidiscip Optim 2013;48(1):33–47. https://doi.org/10.1007/s00158-012-0880-7. ISSN 1615-1488. URL https://doi.org/10.1007/s00158-012-0880-7.

[4] Deng Shiguang, Suresh Krishnan. Multi-constrained topology optimization via the topological sensitivity. Struct Multidiscip Optim 2015;51(5):987–1001. https://doi.org/10.1007/s00158-014-1188-6. URL https://doi.org/10.1007/s00158-014-1188-6.

[5] Le Chau, Norato Julian, Bruns Tyler, Ha Christopher, Tortorelli Daniel. Stress-based topology optimization for continua. Struct Multidiscip Optim 2010;41(4):605–20. https://doi.org/10.1007/s00158-009-0440-y. URL https://doi.org/10.1007/s00158-009-0440-y.

[6] Lee Kangwon, Ahn Kisoo, Yoo Jeonghoon. A novel p-norm correction method for lightweight topology optimization under maximum stress constraints. Comput Struct 2016;171:18–30. https://doi.org/10.1016/j.compstruc.2016.04.005. ISSN 0045-7949. http://www.sciencedirect.com/science/article/pii/S0045794916301833.

[7] Kiyono CY, Vatanabe SL, Silva ECN, Reddy JN. A new multi-p-norm formulation approach for stress-based topology optimization design. Compos Struct 2016;156:10–9. https://doi.org/10.1016/j.compstruct.2016.05.058. ISSN 0263-8223. http://www.sciencedirect.com/science/article/pii/S0263822316306419. 70th Anniversary of Professor J.N. Reddy.

[8] Verbart Alexander, Langelaar Matthijs, Van Keulen Fred. A unified aggregation and relaxation approach for stress-constrained topology optimization. Struct

Multidiscip Optim 2017;55(2):663–79. https://doi.org/10.1007/s00158-016-1524-0. ISSN 1615-1488. URL https://doi.org/10.1007/s00158-016-1524-0.
[9] Yang Dixiong, Liu Hongliang, Zhang Weisheng, Li Shi. Stress-constrained topology optimization based on maximum stress measures. Comput Struct 2018;198:23–39. https://doi.org/10.1016/j.compstruc.2018.01.008. URL https://www.sciencedirect.com/science/article/pii/S0045794917307435.
[10] Sandilya Kambampati, Justin S Gray, and H Alicia Kim. Level set topology optimization of structures under stress and temperature constraints. Computers & Structures, 235:106265, 2020. doi:https://doi.org/10.1016/j.compstruc.2020.106265. URL https://www.sciencedirect.com/science/article/pii/S0045794920306687.
[11] Lund Erik, Stegmann Jan. On structural optimization of composite shell structures using a discrete constitutive parametrization. Wind Energy 2005;8(1):109–24. https://doi.org/10.1002/we.132. URL https://onlinelibrary.wiley.com/doi/abs/10.1002/we.132.
[12] Sjølund JH, Lund E. Structural gradient based sizing optimization of wind turbine blades with fixed outer geometry. Compos Struct 2018;203:725–39. https://doi.org/10.1016/j.compstruct.2018.07.031. ISSN 0263-8223. http://www.sciencedirect.com/science/article/pii/S0263822318306883.
[13] Anderson Evan M, Bhuiyan Faisal Hasan, Mavriplis Dimitri J, Fertig III Ray S. Adjoint-based high-fidelity structural optimization of wind-turbine blade for load stress minimization. AIAA J 2019;57(9):4057–70. https://doi.org/10.2514/1.J057756.
[14] Wook Lee Jong, Kim Jong Jin, Yoon Gil Ho. Stress constraint topology optimization using layerwise theory for composite laminates. Compos Struct 2019;226:111184. doi: 10.1016/j.compstruct.2019.111184. ISSN 0263-8223. http://www.sciencedirect.com/science/article/pii/S0263822318335724.
[15] Montemurro Marco, Catapano Anita. A general b-spline surfaces theoretical framework for optimisation of variable angle-tow laminates. Compos Struct 2019;209:561–78. https://doi.org/10.1016/j.compstruct.2018.10.094. ISSN 0263-8223. https://www.sciencedirect.com/science/article/pii/S0263822318324334.
[16] Catapano Anita, Montemurro Marco. On the correlation between stiffness and strength properties of anisotropic laminates. Mech Adv Mater Struct 2019;26(8):651–60. https://doi.org/10.1080/15376494.2017.1410906.
[17] Izzi Michele Iacopo, Catapano Anita, Montemurro Marco. Strength and mass optimisation of variable-stiffness composites in the polar parameters space. Struct Multidiscip Optim 2021;64(4):2045–73. https://doi.org/10.1007/s00158-021-02963-7.
[18] Catapano Anita, Montemurro Marco. Strength optimisation of variable angle-tow composites through a laminate-level failure criterion. J Optim Theory Appl 2020;187(3):683–706. https://doi.org/10.1007/s10957-020-01750-6.
[19] Setoodeh Shahriar, Abdalla Mostafa M., IJsselmuiden Samuel T., Gürdal Zafer. Design of variable-stiffness composite panels for maximum buckling load. Compos Struct 2009;87(1):109–117. doi:https://doi.org/10.1016/j.compstruct.2008.01.008. URL https://www.sciencedirect.com/science/article/pii/S0263822308000135.
[20] IJsselmuiden Samuel T, Abdalla Mostafa M, Gürdal Zafer. Optimization of variable-stiffness panels for maximum buckling load using lamination parameters. AIAA J 2010;48(1):134–143. URL https://doi.org/10.2514/1.42490.
[21] Dillinger JKS, Klimmek Thomas, Abdalla Mostafa M, Gürdal Zafer. Stiffness optimization of composite wings with aeroelastic constraints. J Aircraft 2013;50(4):1159–68. https://doi.org/10.2514/1.C032084.
[22] Abdalla Mostafa M, Setoodeh Shahriar, Gürdal Zafer. Design of variable stiffness composite panels for maximum fundamental frequency using lamination parameters. Compos Struct 2007;81(2):283–91. https://doi.org/10.1016/j.compstruct.2006.08.018. URL https://www.sciencedirect.com/science/article/pii/S0263822306003278.
[23] Hao Peng, Yuan Xiaojie, Liu Hongliang, Wang Bo, Liu Chen, Yang Dixiong, Zhan Shuangxi. Isogeometric buckling analysis of composite variable-stiffness panels. Compos Struct 2017;165:192–208. https://doi.org/10.1016/j.compstruct.2017.01.016. ISSN 0263-8223. URL http://www.sciencedirect.com/science/article/pii/S0263822316325466.
[24] Peeters Daniël MJ, Lozano Gustavo Gonzalez, Abdalla Mostafa M. Effect of steering limit constraints on the performance of variable stiffness laminates. Comput Struct 2018;196:94–111. doi: 10.1016/j.compstruc.2017.11.002. https://www.sciencedirect.com/science/article/pii/S004579491730411X.
[25] Hong Zhi, Peeters Daniël, Turteltaub Sergio. An enhanced curvature-constrained design method for manufacturable variable stiffness composite laminates. Comput Struct 2020;238:106284. https://doi.org/10.1016/j.compstruc.2020.106284. URL https://www.sciencedirect.com/science/article/pii/S0045794920300870.
[26] Hong Zhi . Optimal Design of Structures and Variable Stiffness Laminates with Strength and Manufacturing Constraints. PhD thesis, Delft University of Technology; 2020.
[27] Mehrotra Sanjay. On the implementation of a primal-dual interior point method. SIAM J Optim 1992;2(4):575–601. https://doi.org/10.1137/0802028.
[28] Svanberg Krister. A class of globally convergent optimization methods based on conservative convex separable approximations. SIAM J Optim 2002;12(2):555–73. https://doi.org/10.1137/S1052623499362822.
[29] Tsai Stephen W, Pagano Nicholas J. Invariant properties of composite materials. Technical report, Air Force Materials Lab Wright-Patterson Afb Ohio; 1968.
[30] Hao Peng, Dachuan Liu Yu, Wang Xuanxiu Liu, Wang Bo, Li Gang, Feng Shaowei. Design of manufacturable fiber path for variable-stiffness panels based on lamination parameters. Compos Struct 2019;219:158–69. https://doi.org/10.1016/j.compstruct.2019.03.075. URL https://www.sciencedirect.com/science/article/pii/S0263822319302764.
[31] Jones Robert M. Mechanics of composite materials. CRC press; 1998. doi: https://doi.org/10.1201/9781498711067.
[32] Scardaoni Marco Picchi, Montemurro Marco. Convex or non-convex? on the nature of the feasible domain of laminates. Eur J Mech - A/Solids 2021;85:104112. doi:https://doi.org/10.1016/j.euromechsol.2020.104112. ISSN 0997-7538. URL https://www.sciencedirect.com/science/article/pii/S0997753820305003.
[33] Van Campen JMJF. Optimum lay-up design of variable stiffness composite structures. PhD thesis, Delft University of Technology; 2011.
[34] Kikuchi Fumio, Okabe Masayuki, Fujio Hidehiro. Modification of the 8-node serendipity element. Comput Methods Appl Mech Eng 1999;179(1):91–109. https://doi.org/10.1016/S0045-7825(99)00031-6. URL https://www.sciencedirect.com/science/article/pii/S0045782599000316.
[35] Khani Ali. Optimum design of steered fiber composite cylinders with arbitrary cross-sections. PhD thesis, Delft University of Technology; 2013. URL https://doi.org/10.4233/uuid:6d9c2f9e-358f-4398-8daa-c37004c816ae.
[36] Nagy Attila P, Abdalla Mostafa M, Gürdal Zafer. On the variational formulation of stress constraints in isogeometric design. Comput Methods Appl Mech Eng 2010;199(41):2687–96. https://doi.org/10.1016/j.cma.2010.05.012. ISSN 0045-7825. URL http://www.sciencedirect.com/science/article/pii/S0045782510001611.
[37] Peeters Daniël MJ, Hesse Simon, Abdalla Mostafa M. Stacking sequence optimisation of variable stiffness laminates with manufacturing constraints. Compos Struct, 2015;125(Supplement C): 596–604. doi: 10.1016/j.compstruct.2015.02.044. ISSN 0263-8223. http://www.sciencedirect.com/science/article/pii/S0263822315001233.
[38] Peeters Daniël, Abdalla Mostafa. Optimization of ply drop locations in variable-stiffness composites. AIAA J 2016:1760–8. https://doi.org/10.2514/1.J054369.
[39] Peeters Daniël, Hong Zhi, Abdalla Mostafa. A compliance approximation method applied to variable stiffness composite optimisation. Struct Multidiscip Optim Nov 2018;58(5):1981–2001. https://doi.org/10.1007/s00158-018-2007-2.
[40] Z. Hong and M.M. Abdalla. Efficient sizing of structures under stress constraints. National Technical University of Athens, 2016.
[41] Attila P. Nagy, Samuel T. IJsselmuiden, and Mostafa M. Abdalla. Isogeometric design of anisotropic shells: Optimal form and material distribution. Computer Methods in Applied Mechanics and Engineering, 264:145 – 162, 2013. doi: https://doi.org/10.1016/j.cma.2013.05.019. ISSN 0045-7825. URL http://www.sciencedirect.com/science/article/pii/S0045782513001461.
[42] Ali Khani, Samuel T. IJsselmuiden, Mostafa M. Abdalla, and Zafer Gürdal. Design of variable stiffness panels for maximum strength using lamination parameters. Composites Part B: Engineering, 42(3), 546–552, 2011b. doi: 10.4233/uuid:6d9c2f9e-358f-4398-8daa-c37004c816ae.
[43] Duysinx P, Bendsøe MP. Topology optimization of continuum structures with local stress constraints. Int J Numer Meth Eng 1998;43(8):1453–78. https://doi.org/10.1002/(SICI)1097-0207(19981230)43:8<1453::AID-NME480>3.0.CO;2-2.
[44] Kraft D. A software package for sequential quadratic programming. Technical report, DLR German Aerospace Center — Institute for Flight Mechanics, 1988.
[45] Roiné T, Montemurro M, Pailhès J. Stress-based topology optimization through non-uniform rational basis spline hyper-surfaces. Mech Adv Mater Struct 2021:1–29. https://doi.org/10.1080/15376494.2021.1896822.